The galaxy populations from the centers to the infall regions in $z \approx 0.25$ clusters[⋆]

M. Verdugo[1], B. L. Ziegler[1,2,3][⋆⋆] and B. Gerken[4][⋆⋆]

[1] Institut für Astrophysik Göttingen, Georg-August Universität Göttingen, Friedrich-Hund-Platz 1, 37077, Göttingen, Germany
e-mail: mverdugo@astro.physik.uni-goettingen.de
[2] European Southern Observatory, Karl-Schwarzschild-Strasse 2, 85748, Garching bei Muenchen, Germany
[3] Argelander-Institut für Astronomie, Universität Bonn
[4] Oxford Astrophysics, Department of Physics, University of Oxford, Keble Road, Oxford, OX1 3RH, UK.

ABSTRACT

Context. In the local universe, the relative fractions of galaxy types differs in galaxy clusters in comparison to the field. Observations at higher redshift provide evidence that cluster galaxies evolve with lookback time. This could be due either to the late assembly of clusters, which is predicted by bottom-up scenarios of structure formation, or to cluster-specific interaction processes.
Aims. To disentangle various effects, we explore the evolutionary status of galaxies from the center of clusters out to their infall regions in $z \approx 0.25$ clusters.
Methods. We conducted a panoramic spectroscopic campaign with MOSCA at the Calar Alto observatory. We acquired low-resolution spectra of more than 500 objects. Approximately 150 of these spectra were of galaxies that are members of six different clusters, which differ in intrinsic X-ray luminosity. The wavelength range allows us to quantify the star formation activity by using the [OII] and the Hα emission lines. This activity is examined in terms of the large-scale environment expressed by the clustercentric distance of the galaxies as well as on local scales given by the spatial galaxy densities.
Results. The general decline in star-formation activity observed for galaxies inside nearby clusters is also seen at $z \approx 0.25$. A global suppression of star-formation is detected in the outskirts of clusters, at about $3R_{virial}$, where the galaxy densities are low and the intra-cluster medium is very shallow. Galaxies with ongoing star-formation have similar activity, regardless of the environment. Therefore, the decline of the star-formation activity inside the investigated clusters is driven mainly by the significant change in the fraction of active versus passive populations. This suggests that the suppression of the star-formation activity occurs on short timescales. We detect a significant population of red star-forming galaxies whose colors are consistent with the red-sequence of passive galaxies. They appear to be in an intermediate evolutionary stage between active and passive types.
Conclusions. Since a suppression of star-formation activity is measured at large clustercentric distances and low projected densities, purely cluster-specific phenomena cannot fully explain the observed trends. Therefore, as suggested by other studies, group preprocessing may play an important role in transforming galaxies before they enter into the cluster environment. Since models predict that a significant fraction of galaxies observed in the outskirts may have already transversed through the cluster center and intracluster media, the effects of ram-pressure stripping cannot, however, be neglected; this is, in addition, true because ram-pressure stripping may even be effective, under certain conditions, inside group environments.

Key words. galaxies: clusters: general – galaxies: evolution – galaxies: stellar content – galaxies: distances and redshifts

1. Introduction

The study of the galaxy population inside clusters dates back to Hubble (1936), who noted that cluster of galaxies are dominated by elliptical and lenticular galaxies, and the surrounding field by spirals. Several modern studies have quantified this effect (*e.g.* Dressler 1980; Goto et al. 2003), which is now known as the morphology-density relation. It has been suggested that spiral galaxies are being transformed into S0s by cluster-specific processes. Further evidence is provided by Dressler et al. (1997),

who noted that the fraction of S0 galaxies decrease strongly at moderate redshifts with spiral galaxies filling the gap.

Since galaxy types correlate strongly with spectral properties, similar behaviors have been found. for colour and spectroscopic data. For example, (Butcher & Oemler 1978) noted an increase in the blue-galaxy fraction inside clusters at intermediate redshifts. This result has been confirmed by many subsequent studies (*e.g.* Kodama & Bower 2001; Ellingson et al. 2001). Also colors are a strong function of environment (Balogh et al. 2004b) and according to the SDSS-based studies of Hogg et al. (2003) and Blanton et al. (2005) broad-band colors correlate more strongly with environment than morphology, breaking in part the degenerate effect of different physical properties and indicating that the processes that change the stellar population properties are acting on different timescales than those that transform the galactic structure.

However, colors can be unreliable indicators of current star formation. Galaxies may have already shut down their star-formation activity and still show blue colors as evidence of previous activity (*e.g.* Kauffmann 1996; Ellingson et al. 2001).

Although, models predict that when a galaxy quenches its star-formation it moves onto the red-sequence quite rapidly (∼400 Myr, Harker et al. 2006). Evidence of this is provided by the strong bimodality observed in galaxy colors (*e.g.* Balogh et al. 2004b), which cannot be simply explained otherwise.

The question about the environmental dependence of galaxy physical properties can be addressed by studies that use more reliable indicators, such as emission lines. Those studies find strong correlations between star-formation activity and galaxy environment (*e.g.* Balogh et al. 1999; Lewis et al. 2002; Gómez et al. 2003; Pimbblet et al. 2006; Haines et al. 2007). Furthermore, these relations do not appear to depend on the mass of the system in which the galaxies are embedded (Popesso et al. 2007).

Since the hierarchical mass assembly with time is a natural prediction of ΛCDM cosmologies, it is obvious to link the decline of the volume-averaged star-formation rate (Hopkins 2004 and references therein) and the galaxy evolution in general to the growth of structure. However, the relative importance of the different processes that act, is not yet clear.

Observations suggest that, at least, two different phenomena are required. One process acts on the stellar populations to terminate the star-formation activity and another process changes the galaxy structure. Ram-pressure stripping (*e.g.* Quilis et al. 2000) is known to be very effective in removing the galaxy cold gas and thus quenching the star-formation activity, but only works under special conditions present in cluster cores where the intracluster gas density and the relative galaxy velocities are high. The softer variant of ram-pressure stripping, strangulation or starvation (*e.g.* Bekki et al. 2002), removes the thin gaseous halo present around galaxies, and the star-formation continues until the remaining disk gas is consumed.

Other possible mechanisms are galaxy-galaxy merging and low-velocity galaxy interactions that trigger an episode of high star-formation, which consumes a high fraction of gas in a short time and may stripp the remaining via gravitational shocks and feedback processes (*e.g.* Larson & Tinsley 1978; Bekki 2001). This may provide explanation to modern observations where the decrease of star formation activity has been detected already at very low galaxy densities (Lewis et al. 2002; Gómez et al. 2003). However, other mechanisms are necessary to explain the change in morphology. Mergers are known to be efficient in changing late-type galaxies into ellipticals (Toomre et al. 1977; Hernquist 1992), but the relative velocities must be low, which is not the case in clusters. But the galaxy structure can be changed on longer timescales by harassment (Moore et al. 1998) due to high-velocity encounters between cluster galaxies (see also Gnedin 2003).

Despite the accumulation of observational evidence over the years, the link between the growth of structure with time and galaxy evolution remains elusive and the fundamental questions remain unanswered. How rapidly and significantly is supressed the star-formation activity in infalling galaxies? What exactly is the environmental dependence of the star-formation activity? Is it suppressed mainly due to local or global processes? What is the predominant mechanism?

Studying clusters at higher redshift may provide new clues about the processes involved, because the global star-formation activity was higher in the past and clusters show at all redshift much lower activity when compared with the surrounding field (*e.g.* Balogh et al. 1999). Models also predict that in the past the galaxy-infalling rate must have been higher (*e.g.* Bower 1991). The processes at work must therefore have been increasingly more effective at increasingly higher redshift, and at higher redshift the probability of observing the processes in action, increases.

Several studies at higher redshift have focused on the central parts of clusters (*e.g.* Balogh et al. 1999, 2002a; Poggianti et al. 2006), but, as studies at $z \approx 0$ show, the relation between star-formation activity and density is already discernible at low galaxy densities, inside the infalling regions where the galaxies, which are infalling from the field, may begin to experience the influence of cluster, and interactions become more frequent.

Even in the distant universe, clusters of galaxies project a large solid angle, and wide-field observations are therefore required. The contamination due to foreground and background objects is larger,

We report the results of a project to study galaxy evolution from the infalling regions to the cluster centers, covering projected radial distances out to 4 virial radii for six clusters at $\langle z \rangle \approx 0.25$. First results for two clusters were already published by Gerken et al. (2004). In Sect. 2 we describe the observations as well as the method used to measure the important parameters of the galaxies. In Sect. 3 we describe cluster identification and other general properties including the environmental definition. In Sect. 4 we describe in detail each observed field. In Sect. 5 we show the main results, discussing their implications in Sect. 6. In Sect. 7 we explore some properties of the star-forming population. Our summary and conclusions are provided in Sect. 8.

Throughout this paper, we use a cosmology of $H_0 = 70$ km s^{-1}Mpc^{-1}, $\Omega_m = 0.3$ and $\Omega_\Lambda = 0.7$.

2. The data

2.1. Cluster selection

The sample was selected from the X-ray Dark Cluster Survey (XDCS, Gilbank et al. 2004) whose aim was to compare X-ray and optical identification algorithms of clusters. For this purpose, deep, optical imaging of RIXOS fields (Mason et al. 2000) was acquired, which were imaged in the X-ray by the ROSAT Position Sensitive Proportional Counter (PSPC). Some of the X-ray data were also analyzed by Vikhlinin et al. (1998), and later by Mullis et al. (2003), from which the X-ray fluxes were taken. The XDCS provides us with V and I-band photometry taken with the Wide Field Camera (WFC) at the Isaac Newton telescope (La Palma, Spain). This camera has a field of view (FOV) of 34×34 arcmin.

We selected for follow-up spectroscopy three fields containing, in projection, two clusters each, thus increasing the probability of targeting a cluster member. The clusters have a wide range of X-ray luminosities and probably different evolutionary states. They are at similar redshifts, making them good candidates to probe evolution uniquely due to environmental effects at a cosmological epoch with look-back times of ∼3.0 Gyr.

A summary of the cluster properties can be found in Table 1. Details of how the different quantities were calculated are described in the forthcoming sections.

2.2. Observations

The spectroscopy was performed with the multi-object spectrograph MOSCA mounted at the 3.5 meters telescope at Calar Alto Observatory[1] (Spain). These observations were carried out in two runs, from 10 to 15 February and 20 to 24 March, 2002.

---

[1] CAHA, Centro Astronomico Hispano Alemán.

Table 1. Main parameters for the cluster sample. The cluster denominations come from Vikhlinin et al. (1998) (VMF) and Gilbank et al. (2004) (XDCS). Coordinates are given with respect to the X-ray centroid. X-ray fluxes are taken from Mullis et al. (2003). R_{virial} is the virial radius and σ the velocity dispersion. N is the number of members identified in each cluster.

Field	Cluster	Alternative name	RA	DEC	z	f_X [10^{-14} ergs/s cm^2]	$L_{X,bol}$ [10^{43} ergs/s]	σ [km/s]	R_{virial} [Mpc]	N
R220	VMF194	RX J1729.0+7440	17:29:02	74:40:46	0.210	17.3	5.01	282±52	0.742	8
	XDCS220	cmJ172333+744410[a]	17:23:33	74:44:10	0.261	0.3	0.14	621±271[b]	1.535	15
R265	VMF131	RX J1309.9+3222	13:09:56	32:22:31	0.294	9.0	6.03	476±110	1.132	29
	VMF132	RX J1313.2+3229	13:11:13	32:28:58	0.247	46.7	24.5	774±150	1.945	18
R285	VMF73	RX J0943.5+1640	09:43:32	16:40:02	0.254	23.1	12.3	661±65	1.647	44
	VMF74	RX J0943.7+1644	09:43:45	16:44:20	0.180	21.2	4.79	481±79	1.313	34

[a] Gilbank et al. (2004)

[b] This value is likely overestimated, since the cluster does not seem to be in dynamical equilibrium, see text for details

Each field was observed using 7–8 slit masks, each covering ~11×11 arcmin FOV, therefore the original WFC fields are adequately covered by the spectroscopic observations. Each MOS mask contains 20 to 30 slits of ~25 arcsec of length to subtract the sky accurately.

We used the low-resolution grism GREEN_500, which encompasses a wide wavelength range, from 4300 Å to 8200 Å, allowing us to study both the [OII]λ3727 and the Hα emission lines, at the targeted redshifts, which are critical to study star-formation activity in galaxies. The grism provides a spectral resolution of $R \sim 10 - 15$ Å, which corresponds in the rest-frame to $8 - 12$ Å, for our slit width of 1 arcsec.

The exposure times ranged between one and three hours depending on the apparent magnitudes of the objects selected. In a few cases these times were increased to account for variations in the weather. The magnitude distribution of the final sample in Fig. 1. The selection of objects for spectroscopy was based only on their *I*-band magnitudes to avoid any color bias. Additional restrictions were imposed by masks geometry.

In total, 537 spectra were acquired. For our analysis, we included in addition 21 spectra from our previous projects "Low X-ray luminosity clusters" (Balogh et al. 2002a) in the R265 field and "X-dark cluster survey" (Gilbank et al. 2004) in the R220 field. This was possible because those spectra were observed using a similar instrumental setup. However, we reexamined all spectra to be able to apply the same criteria for the whole sample. Finally, we found that 297 spectra were suitable for analysis (see below for the precise criteria used).

2.3. Data reduction

Our data reduction procedures were described in Gerken et al. (2004) and can be summarized by the following steps: Bias subtraction, extraction of individual slits, correction of the distortion induced by the focal reducer in MOSCA, flat-fielding, sky subtraction, extraction of the one-dimensional spectra, wavelength calibration, and combination of the individual exposures.

All of these tasks were performed within the MIDAS[2] environment, interactively, using custom-made routines. Each spectrum was visually-inspected to detect pecularities that may affect the measurements.

[2] MIDAS, the Munich Image Data Analysis System is developed and maintained by the European Southern Observatory (ESO)

2.4. Individual redshift determination

Individual galaxy redshifts were determined by fitting a Gaussian profile to a set of prominent emission and absorption lines ([OII]λ3727, CaK, G-band, Hβ, [OIII]λ5007, Mgb, Fe5335, NaD and Hα). For each galaxy, we defined the galaxy redshift to be the mean value of the individual line redshifts; we note that not all lines were always visible in each galaxy spectrum. The redshift error was the standard deviation of the redshift determined from at least four clearly-identifiable lines.

We assigned to each spectrum a number representative of its quality, based on how clearly the lines could be seen in comparison to the continuum noise, how many lines were visible or whether the lines were contaminated by artifacts. Spectra designated with a quality 0 (zero) were of the highest quality and those with 7 (seven) the poorest. Spectra of a quality value of above 3 (three) were, in general, considered not trustworthy and were excluded from our final analysis.

Redshifts and other parameters for individual galaxies are provided in Table 3, which is only available *online*.

2.5. Quality and completeness

We recognize that to assign a quality number based on eye perception may be highly subjective. The main risk is an over-representation of star-forming galaxies, since emission lines are easily visible and identifiable. Those galaxies have a greater chance to be included in the final sample, although they can be systematically fainter than passive galaxies. To test for a presence a a bias, an accurate estimation of the continuum noise is required.

Each spectrum was normalized by a polynomial fit to the continuum, in the range of interest, from [OII] to Hα. In the normalized spectra, the standard deviation was calculated, using a 3-σ clipping algorithm over five iterations, as an estimation of the continuum noise.

The algorithm used to fit the polynomial ignored emission lines and other small-scale prominent features, such as sky-line residuals and telluric lines. We present in Fig. 2 our measurements of continuum noise as a function of V-band apparent magnitude, which is a measure of the total flux. Although the selection of the objects for observing was made using *I*-band magnitudes, the *V*-band magnitudes provide a more accurate measure of the galaxy continuum in the spectroscopic wavelength range of interest and provides a good estimation of the total flux. No
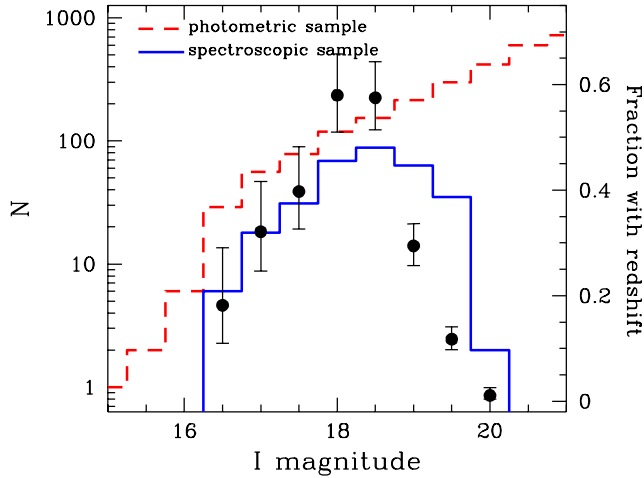
Fig. 1. The combined selection function for the whole sample. The histograms show the I-band magnitude distribution for the photometric (dashed red line) and spectroscopic (blue solid line). The points show the fraction of galaxies for which we derived redshifts. The error bars are Poisson distributed errors (Gehrels 1986).

Fig. 2. V-band apparent magnitude versus continuum signal-to-noise ratio as measured in Sect. 2.5. Open red diamonds are galaxies without emission lines, whereas filled blue diamonds are galaxies with at least one emission line.

significant difference in the distribution of star-forming versus passive galaxies was observed, with the exception of two faint star-forming galaxies.
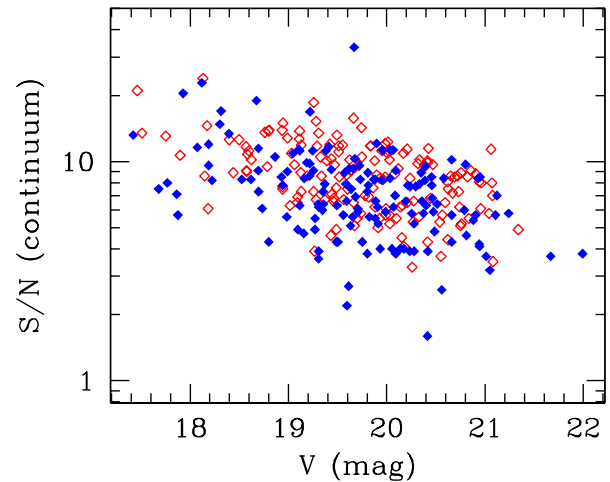
2.6. Selection function

In all fields, only a fraction of the galaxies below our spectroscopic limit ($I \approx 19.5$ mag) was observed. Therefore, selection effects may be present and need to be corrected. This is achieved by constructing a selection function. However, as part of the fields were covered by a different number of slit masks (some had only one, others two), and the galaxy distribution is not uniform across the field, we developed two selection function for each field taken into consideration these effects.

The individual selection functions were calculated by counting the number of objects with successful spectroscopy (*i.e.* reliable redshifts) versus the number of photometrically detected objects up to the spectroscopic limit ($I \approx 19.5$) inside the areas covered by the corresponding spectroscopic masks, in different magnitude bins. No background correction was applied, because we only needed to know the relative number of photometrically and spectroscopically observed galaxies to evaluate the success of our spectroscopy (see also Sect. 2.4). The resulting functions were applied to the cluster galaxies in the form of weights to the statistical properties of the cluster galaxies. The combined selection function is shown in Fig. 1. However, some tests have shown us that the results depend little on the weighting applied and are robust against other considerations.

2.7. Equivalent widths and star-forming galaxies

We use equivalent widths (hereafter EWs) as a measure of the line strengths of the absorption and emission lines. We measured EWs automatically using a custom-made routine, which automatically corrects for the effects of cosmic expansion. In the case of [OII] and Hα, which are used as tracers of ongoing star formation, we adopted the definition given by Balogh et al. (1999). We adopt the convention that typical emission lines are

shown with positive values when detected, but also, that typical absorption lines (*e.g.* Hδ) are positive in absorption.

The Hα definition used, effectively isolates the targeted line from the adjacent [NII] (which was also measured). Each spectrum was visually inspected to find out whether any lines fell into the prominent telluric bands (A & B), were affected by sky-subtraction residuals or by artifacts in the spectra. In some cases, the lines were flagged and not used in subsequent analyses.

Usually the minimum EW that could be reliably measured was 5 Å (see Balogh et al. 2002a for a demonstration based on similar data), therefore galaxies with equivalent widths $W_0 > 5$ Å, either in [OII] or Hα (or both), are considered star forming galaxies. We will show later in this paper (in Sect. 7 and in the Appendix A) that this classification is robust and physically meaningful.

2.8. Absolute magnitudes

We use the software KCORRECT (Blanton & Roweis 2007) to calculate k-corrections and thus absolute magnitudes for galaxies in our spectroscopic sample. This code is based on the latest stellar population models of Bruzual & Charlot (2003) and photoionization models of Kewley et al. (2001). As a byproduct of the k-correction, the code also derives stellar masses, which will be used in Sect. 7.

The fields R265 and R285 were also imaged by SDSS[3] (York et al. 2000), therefore, we can use the advantage of multicolor photometry. Unfortunately, the remaining field (R220) was not observed by the SDSS and we have to use the available V and I-band magnitudes provided by Gilbank et al. (2004) and therefore, larger uncertainties are expected in the calculations. However, we can test the accuracy of the magnitudes by comparing the results obtained using the two-band photometry and the multi-band photometry in the other two fields. For our analysis, we obtained B, V and R rest-frame absolute magnitudes (in the Vega system using Johnson-filter definitions).

We found scatters of ~0.2 mag and offsets of ~0.15 mag between the magnitudes obtained in either way. The offsets depend

---

[3] Sloan Digital Sky Survey, http://www.sdss.org
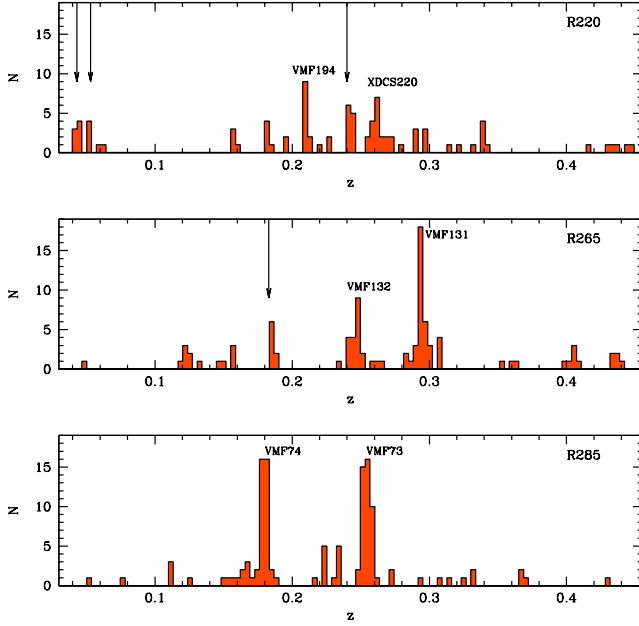
Fig. 3. Redshift distribution of the targets in the three fields, with the cluster names marked. The small arrows mark the position of the group candidates (see Sect. 4).

Fig. 4. Color-magnitude diagrams of the members of the six observed clusters. Filled blue diamonds are star-forming galaxies, whereas open red diamonds are passive galaxies. The shaded areas are defined by the 3-σ deviation of the least squares fits to the passive galaxies. The vertical dashed line mark $M_I \approx -21.4$ used in the density calculation (see Sect. 3.5). We note the red star-forming galaxies belonging to the red-sequence and even redder in some of the clusters.

on redshift and can be corrected using a linear fitting. The scatter is in agrees with values found by Blanton et al. (2005) for transformations between different filter systems. These differences are small and hardly change the conclusions in this study.
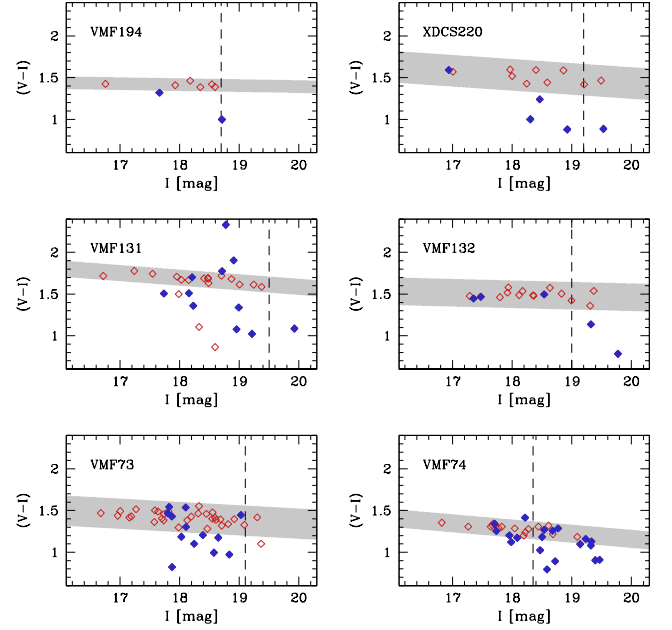
We selected the original absolute magnitudes calculated using the SDSS photometry for the R265 and R285 fields and applied the redshift correction for the galaxies in R220 to only the magnitudes derived using the V and I-band photometry. All apparent magnitudes were corrected for Galactic extinction using the maps of Schlegel et al. (1998). No correction for internal absorption was attempted, since we do not have information, in many cases, about galaxy inclination, and the Balmer decrement cannot be used in all cases because Hβ is rarely detected for emission lines galaxies, and uncertainties for passive galaxies will remain. No important differences were found between the absolute magnitude distributions for the field and cluster sample.

The stellar masses were tested against the formulae of Bell et al. (2005) using our restframe B and V-band magnitudes. We found deviations only at the high mass end. Since the KCOR-RECT code is reliable in predicting magnitudes between the SDSS and our system, we preferred to use its data outputs.

3. The clusters

3.1. Cluster membership

In each field, the redshift distribution was analyzed to detect prominent structures. The clusters studied had already known redshifts, with the exception of those in the R220 field whose redshifts were unclear (see Sect. 4 for details), but were confirmed. The mean cluster redshift (z) and velocity dispersion (σ) were calculated using the bi-weight estimators of Beers et al. (1990) and iteratively excluding galaxies beyond 3-σ of the mean redshift until the solution converged. We applied a boot-

strapping technique to check the stability of the results and calculate the errors in the velocity dispersion. The results can be found in Table 1 and the redshift distribution in Fig. 3.

3.2. Galaxy colors

We use the spectroscopic information to separate the galaxy population. Galaxies with emission lines are considered star-forming and those without emission, passive (see Sect. 2.7). Plotting the $V - I$ color versus I-band magnitude (Fig. 4) for cluster galaxies shows that all clusters have clear red-sequences. Only few cluster galaxies have blue colors but no emission lines.

The distribution of the passive galaxies, the red-sequence, is well described by simple least-squares fits. The weighted mean dispersion of the red-sequences is $\sigma \approx 0.05$ mag, which is the typical error in the photometry. All galaxies redder than the lower 3-σ limit are considered red galaxies, and blue otherwise. Given this criterion, we note the existence of a population of red star-forming galaxies belonging to the red-sequence and even redder. More striking is the high number of those galaxies belonging to the cluster VMF74. Some of the characteristics of this sub-population will be described in Sect. 7.

3.3. X-ray luminosities

The X-ray luminosities of the intracluster medium and cluster velocity dispersions are indicators of cluster masses. The correlation between these two parameters has been extensively studied (*e.g.* Markevitch 1998; David et al. 1993; Xue & Wu 2000) and is interpreted as a sign of dynamical equilibrium, even

Fig. 6. Relation between virial radius and projected density before and after correction for field contamination. The open red circles are passive galaxies, whereas filled blue circles are star-forming galaxies.
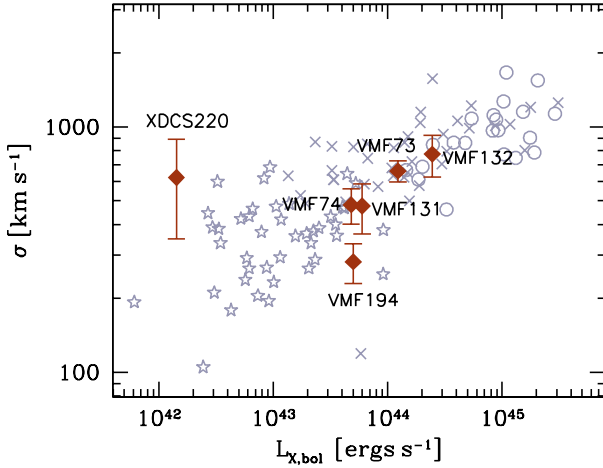
Fig. 5. Bolometric X-ray luminosity plotted against velocity dispersion. Open circles (Markevitch 1998), crosses (David et al. 1993) and stars (Xue & Wu 2000) represent the L_X-σ relation for local clusters. The six clusters studied here are plotted as diamonds with error bars in the velocity dispersion.

though the large scatter in the local relation indicates deviation from this equilibrium. Nevertheless, later studies have found that cluster masses derived from using independent methods, including gravitational weak-lensing, correlate with relative small scatter (*e.g.* Hicks et al. 2006), solving a long-standing controversy.

In Fig. 5, we plot the bolometric X-ray luminosities against the derived velocity dispersions. The clusters follow the local $L_X - \sigma$ relation, with the notable exception of XDCS220, which is underluminous for its velocity dispersion. This cluster displays a tail in the redshift space, which complicates the calculation of the velocity dispersion and implies, therefore, that it is likely overestimated.

In addition, VMF194 is peculiar, because it has a velocity dispersion that is too low for its X-ray luminosity. This effect may come from two different sources. First, σ may be underestimated due to selection effects given the low number of members identified. Second, we detect a background group at $z \approx 0.24$ of a relative large velocity dispersion (see Sect. 4.1), which may have contaminated the X-ray measurements. Nevertheless, this cluster does not appear to be so extremely offset from the $L_X - \sigma$ relation as XDCS220.

With the exception of XDCS220, the cluster X-ray luminosities and velocity dispersions are similar to those of Virgo, A496 and Coma clusters (*e.g.* David et al. 1993; Rines et al. 2003) and thus are expected to be clusters that are as equally massive.

3.4. Virial radius

From the results shown in the previous section, it is possible to assume that the clusters sampled in this study are in general in dynamical equilibrium[4] and therefore, the virial theorem is applicable. The radius within which the virial mass is estimated to be contained is called the virial radius. According to the observationally-calibrated derivations of Carlberg et al. (1997), R_{virial} is defined as the distance where the mean inner cluster density is 200 times the critical density $\bar{\rho}(z)$ of the Universe and
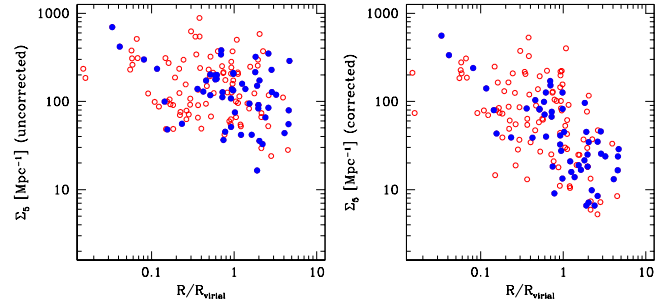
it is also called r_{200}. Its relation to the velocity dispersion σ is given by

$$R_{virial} = r_{200} = \frac{\sqrt{3}}{10} \frac{\sigma}{H(z)} \qquad (1)$$

where $H(z) = H_0 \sqrt{\Omega_m (1 + z)^3 + \Omega_\lambda}$ for a Hubble constant of $H_0 = 70 \, \mathrm{km \, s^{-1} \, Mpc^{-1}}$, $\Omega_\lambda = 0.7$ and $\Omega_m = 0.3$.

Since r_{200} (R_{virial}) characterizes the size of clusters following the assumption of a universal mass profile, it is useful as an environmental indicator of mass density, given the clustercentric distances of cluster galaxies. Therefore the distances of galaxies to the center of the cluster are normalized by the respective cluster virial radius, allowing the entire sample to be combined into a single cluster, increasing the statistical significance of our analysis and reducing the effects of cluster-to-cluster variations.

3.5. Projected density

Another common indicator of environment is the local number projected (2-D) density of galaxies. Its calculation does not make any assumption about the physical properties of the clusters, but other precautions must be taken. First, the galaxy number density is a function of luminosity. The spectroscopic limit of $I \approx 19.5 \, \mathrm{mag}$ corresponds to $M_I \approx -21.4$ for the furthermost cluster ($z \approx 0.3$) and $M_I \approx -20.2$ for the closest one ($z \approx 0.2$), taking in consideration the typical k-corrections (see Fukugita et al. 1995).

For each cluster, the photometric catalog was divided using an apparent magnitude that corresponds on average, to the luminosity limit of the most distant cluster, which translates into an apparent magnitude cut of $I \approx 18.3$ at $z = 0.18$ (see Fig. 4).

The projected density is defined by the area that encircles the fifth nearest neighbor to this galaxy, which is referred as Σ_5. However, significant foreground and background contamination is expected and must be corrected before completing any statistical analyses. In the literature, several methods of different complexity are described to deal with this problem. Most of them subtract a value (local or global) from the calculated density, making different assumptions. However, those methods often yield unphysical values (*i.e.* negative numbers) for the density estimates. Our case is even more complicated, because we do not only have field contamination, but also contamination from the other projected cluster. Therefore, we chose another approach using in combination the photometric and spectroscopic data-set.

---

[4] It is probably not true for XDCS220, however for the sake of comparison it will be assumed that it is. VMF194 is also peculiar, but the differences may arise from another sources.
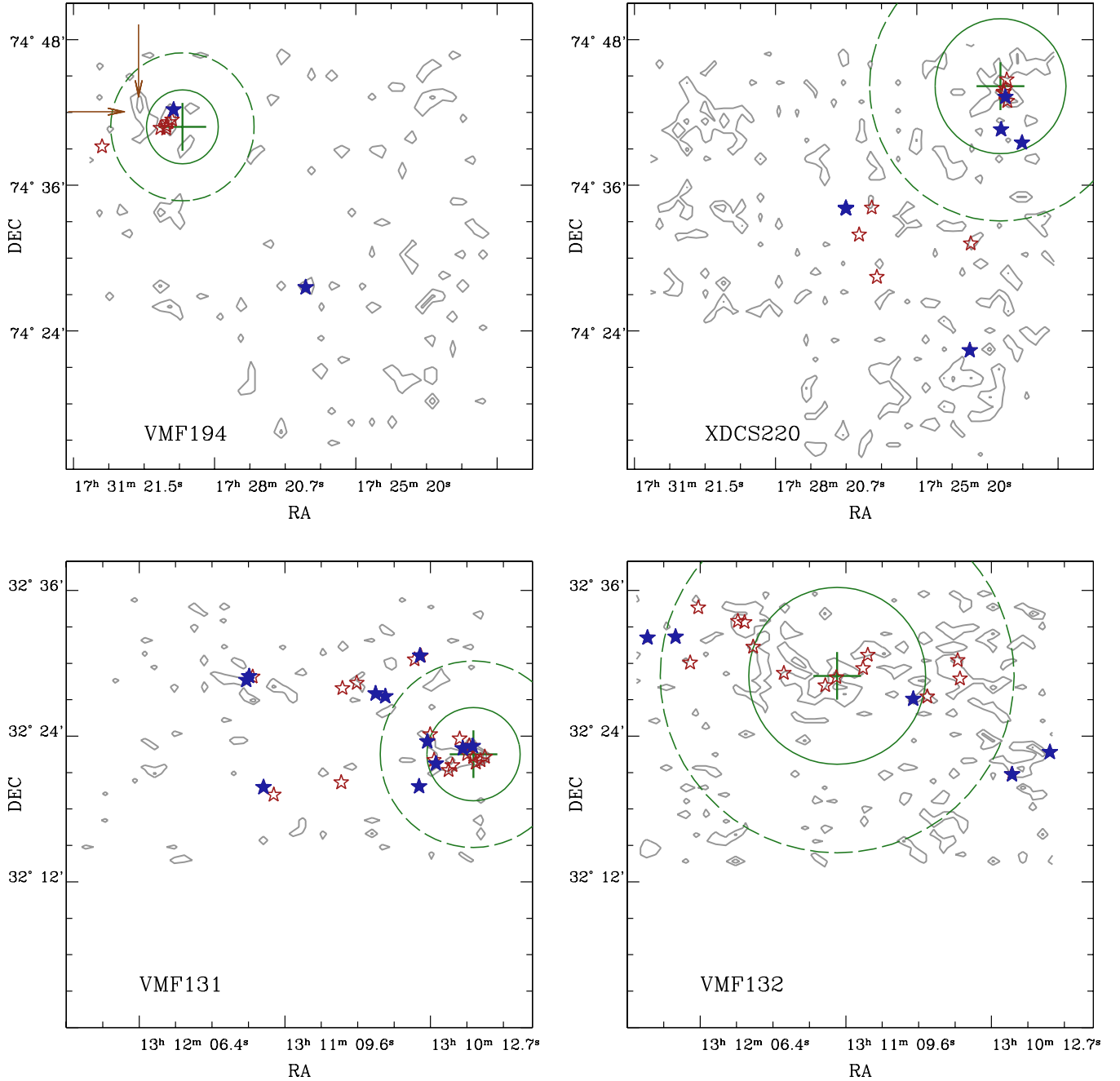
Fig. 7. Representation of the fields of the observed clusters as indicated by the names on the individual figures. Only cluster members are shown. Blue filled and open red symbols represent star-forming and passive galaxies respectively. The cluster centers are marked with large vertical crosses and the large concentric circles represent one and two virial radii respectively. The contours are the density maps of all galaxies with colors compatible with the red-sequence of the respective cluster (see Sect. 4). The arrows in the VMF194 plot indicate the position of a rich background group (see Sect. 4.1).

If the *true* number density of galaxies in a certain region of the cluster is N (unknown) and the observed is M (determined from the photometric catalog and including the contamination), one has a relative fraction of $f = N/M$. From the spectroscopic data set, we know that there are n galaxies belonging to the cluster and m is the number of total observed galaxies in the same area with secure redshifts. Since the selection was performed randomly (based only on I-band magnitudes), we can assume that we have the same fraction expressed now by $f = n/m$, thus

we can correct the observed value M, multiplying it by n/m, obtaining N.

The areas used to make these corrections are larger than the areas considered by the individual density calculations. They encircle always 10 galaxies with secure redshifts, and we count the number of cluster members versus the non-cluster galaxies. Having a high-filling factor helps to the statistical reliability of this simple method, because the areas sampled will have smaller physical sizes and thus smaller deviations from the local density. The results of the correction can be seen in Fig. 6. After this pro-
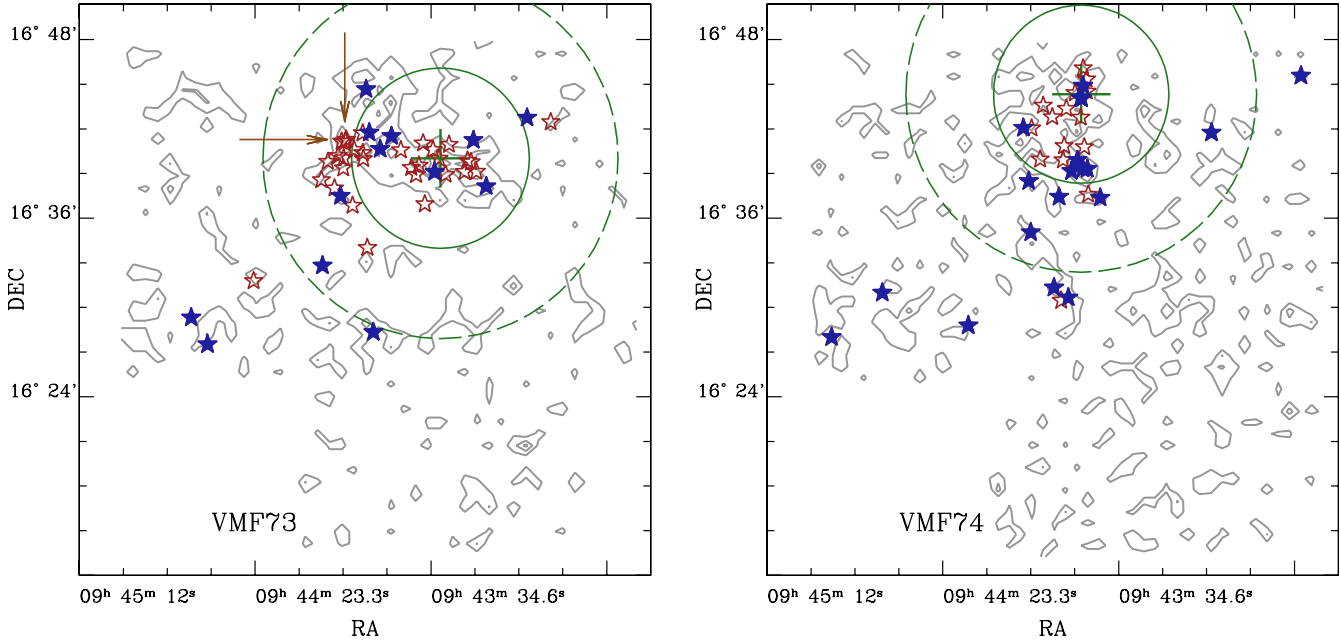
Fig. 7. continued. Representation of the observed clusters as indicated by the names on the individual figures. Only cluster members are shown. Blue filled symbols are star-forming galaxies and open red are passive ones. The arrows in VMF73 show the position of the X-ray structure detected by Rasmussen & Ponman (2004) (see Sect. 4.3).

cess, a correlation between virial radius and projected density becomes evident.

We would like to emphasize that the densities calculated here are not directly comparable to those calculated elsewhere, because the magnitude cuts and approaches to subtract the background vary between different authors.

Finally, galaxies fainter than the individual cluster magnitude cut were not included in the composite cluster; this reduced the final sample size to ~120 galaxies. We note that, many of the galaxies excluded are member of the VMF74 cluster.

4. Description of the fields

We describe each field, providing detail in particular of the general cluster properties, candidate groups, and cluster substructure. Each cluster is represented separately in Fig. 7, with different symbols for star-forming and passive galaxies. The large concentric circles represent one and two virial radii respectively calculated according to Eq. 1.

The contours show the distribution of all galaxies down to $I = 23$ mag with colors similar to the respective red-sequences (see Fig. 4). They provide some information about the spatial distribution of galaxies without spectroscopy. Since the CMR for ellipticals has little scatter, the structures are probably at *similar* redshifts. This technique has been successfully used by other studies to detect substructures around clusters (*e.g.* Kodama et al. 2001; Tanaka et al. 2005). In this case, however, it is not possible to firmly state the significance of those structures because only the $V-I$ color, provided by Gilbank et al. (2004), is used and the red-sequences of each projected cluster have similar colors (see Fig. 4). The use of the SDSS multi-color photometry does not help because their uncertainties are larger at faint luminosities and the red-sequences become completely blended. Therefore, the contours plotted in each figure must be taken only as informative. Nonetheless, many of the spectroscopically iden-

tified members are actually associated with structures that show up using this simple color cut.

4.1. R220

The R220 field is a very complex field. There is, first, a larger number of objects than in the other fields. This is maybe due to its lower galactic latitude. Our photometric catalog was cleaned of star-like objects, but , the separation is not perfect and many of our slits unintentionally contained stars, losing the advantage of having an extra mask for this field (8 instead of 7). The redshift distribution also looks more complex (see Fig. 3), with a number of associations besides the two clusters.

The cluster VMF194 was found to be difficult to confirm optically by Vikhlinin et al. (1998) and collaborators. According to Gilbank et al. (2004), the proposed cluster corresponds to "a very extended X-ray emission and the galaxy over-density is similarly extended". Here, VMF194 at $\langle z \rangle = 0.210$ (see Table 1) was unequivocally detected, but the data obtained showed that the cluster has a surprisingly low velocity dispersion for its X-ray luminosity (see Fig. 5). Three additional galaxies have redshifts that imply cluster membership, according to the previously-measured 3-sigma limits; these galaxies are located, however, at large clustercentric radii ($> 7R_{virial}$). When they are included, the velocity dispersion does not change substantially, and thus they were excluded as members, but not included in the field sample.

At an angular distance of ~4.4 arcmin of VMF194 (*i.e.* almost overlapping positions), we detect a clump of galaxies at redshift $\langle z \rangle = 0.243$. This clump also shows up in the spatial distribution: 8 out of the 11 galaxies are clustered in an area smaller than $\sim 0.3 \times 0.7$ Mpc . The velocity dispersion of this group is $\sigma = 401 \pm 74$ km/s, indicating that it may be quite massive. No red-sequence is detected and 4 out of the 8 galaxies, show star-forming activity. This group may have been the cause of confu-

Table 2. Main parameters for the groups candidates for our fields. Their identification codes show the average positions of the members. Mean redshifts (z) and average deviations are shown as velocities (σ). The biweight estimators were used only in groups with at least 8 members. The group number identify member galaxies in the online table.

Group	ID	$\langle z \rangle$	σ [km s^{-1}]	N
1	r220_1J 172604+742830	0.053	126	4
2	r220_2J 172518+742844	0.043	390	6
3	r220_3J 172958+744204	0.243	401	8 (11)
4	r265_1J 131030+322840	0.186	349	7

Fig. 8. Fraction of blue cluster galaxies (as defined in Sect. 5.1) against normalized virial radius and projected density.

sion in all previous studies in this field. In fact, the concentration of galaxies is more prominent for this group than for VMF194 when selected by a color cut (see Fig. 7).

We confirm the presence of the cluster at $\langle z \rangle$ = 0.261 detected by Gilbank et al. (2004), which is there referred as XDCS cmJ172333+744410 (it is called here XDCS220 for short). We confirm the redshift calculated there. This cluster has a very low X-ray luminosity and passed undetected in the X-ray analysis of Vikhlinin et al. (1998) and Mullis et al. (2003). It displays a large velocity dispersion (see Table 1), which is probably overestimated because of the existence of a tail in redshift space. Excluding members that are located at large clustercentric distances does not change the biweight estimate of the velocity dispersion. We conclude that it is a real feature of the cluster, which is probably in the process of relaxing or has an extended structure along the line of sight. This cluster shows a clear red-sequence and 5 out 14 galaxies show ongoing star-forming activity.

Two other group candidates were found (see Table 2), one at $\langle z \rangle$ = 0.04293 ($\pm$390 km/s) with 6 members in 1 Mpc^2 (or 5 in 0.3$\times$0.7 Mpc), all being star-forming galaxies, and the other is at $\langle z \rangle$ = 0.05274 ($\pm$126 km/s), with four members in 0.3$\times$0.4 Mpc.

4.2. R265

The central parts of the cluster VMF131 were previously observed by Balogh et al. (2002a) as part of their low luminosity X-ray cluster project, where it was known as CL1309+32, using the same instrument and setup; we have therefore added their data into our study. Since, it is the most distant cluster studied, we were able to detect members up to clustercentric distances of $R > 4R_{virial}$. The color contours shows little substructure around the cluster but the central overdensity is clearly visible in Fig. 7.

The cluster VMF132 is the richest cluster in our sample and has the largest velocity dispersion and thus the largest virial radius, occupying a large proportion of the field. In spite of this, the galaxy concentration is clearly irregular when color cuts are applied and only sparse structures are detected.

An extended group was also detected at $\langle z \rangle$ = 0.186 $\pm$ 0.001185 (349 km/s) with 8 members in an area of 1×2 Mpc, or 0.7×1.5 Mpc if one excludes one galaxy.

4.3. R285

The two clusters present in this field almost overlap in their positions on the sky (angular separation ~5 arcmin, see Fig. 7). In addition, we placed more masks in the central parts of the clusters, which led to a higher success rate compared with the other fields. The cluster VMF73 at z = 0.254 has the largest number
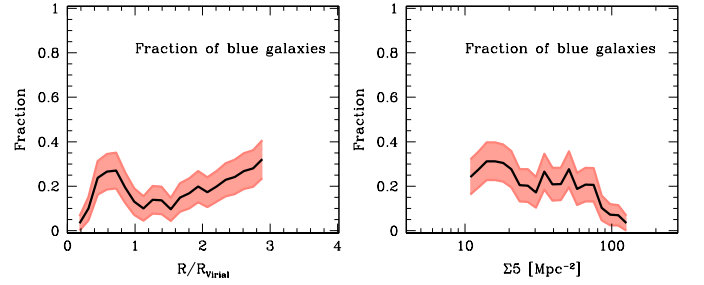
of members identified (N = 44). Most of the identified members of this cluster are located inside 1 R_{virial}, in an elongated structure running approximately in the East-West direction. In fact, when galaxies are selected by the colors of the red-sequence this structure is clearly visible. Unfortunately, the foreground cluster (VMF74) has a CMR with very similar colors (see Fig. 4) and it is not possible to separate clearly both clusters using this technique.

The cluster center is approximately at the middle of this structure, but in one extreme, at a distance $\sim$ 1R_{virial}, a compact group (100$\times$100 kpc^2) of bright, passive galaxies is found. Their positions coincide with the extended X-ray source XMMJ0943.9+1641 detected by Rasmussen & Ponman (2004). The X-ray flux of this structure is $f_{X,1-2\,keV} = 3 \times 10^{-14}$ erg cm^{-2} s^{-1} (Rasmussen, private communication), which yields an X-ray luminosity $L_{X,bol} = 1.38 \times 10^{43}$ erg s^{-1}, assuming that the X-ray structure is associated with the VMF73 cluster. This structure may be the center of a large, newly infalling group of galaxies, although no peculiarities were detected in the redshift distribution.

The cluster VMF74 has a surprisingly large number of star-forming members: 19 out of 34, and many of them have colors similar to the red sequence (see Fig. 4). It is also the closest of the clusters studied with a mean redshift of z = 0.18. The spectroscopically-identified members are also distributed in a elongated structure in an almost North-South direction, although less clear than in VMF73. It also shows up using color cuts. The cluster center lies at the northern extreme of this structure.

According to the *XMM*–Newton X-ray analysis of Rasmussen & Ponman (2004), both VMF clusters do not exhibit peculiarities and are fairly typical for their masses.

4.4. Field sample

The field sample consist of all galaxies between $0.15 < z < 0.35$, with at least 6-σ of distance in the redshift space from the clusters. We included the galaxies belonging to the suspected groups. Since the sample is built using the same observations any comparison is straightforward. The same redshift-dependent magnitude cuts have been applied, which yields 97 galaxies used for direct comparison. Throughout this paper, many quantities will be compared with those of this subset.

5. Analysis of the composite cluster

5.1. Galaxy colors and environment

In Fig. 8, we plot the fraction of blue galaxies (as defined in Sect. 3.2) against our environment indicators. We observe an increase in the fraction in both cases towards large radius and low

density regions, however a notable peak inside $R < 1R_{virial}$ is observed. In the high-density regions, the fraction remains low and is statistically similar for clusters at those redshifts (*e.g.* Ellingson et al. 2001).

The shapes of those trends are similar to the fraction calculated using emission lines as indicators of star-formation activity (Fig. 9), which should not be surprising since bluer colors often reflect the presence of young stellar populations. However, there is an important fraction of star-forming galaxies with red colors, and in principle it may break down the previous relation. They only appear to affect the fraction value, *i.e.* the blue fraction is lower than the star-forming fraction at fixed clustercentric distances and densities, but not the shape of the trends. We investigate this further in forthcoming sections.

The fraction of blue galaxies was calculated over the nearest N galaxies to each point in the plane, *i.e.* inside a moving box containing a fixed number of objects, centered on each galaxy. Making the number N too small increases the noise; making it too large shortens the dynamical range covered, because this method truncates the extremities of the lists. It was found that using the nearest 15–25 points is a good compromise between spatial coverage and stability.

To check the statistical significance, a bootstrap technique with 2000 iterations was applied to each value, taking the mean and the standard deviation of the bootstrapped values (checking previously if the distributions are compatible with Gaussian) as the final values and their errors, respectively.

Noise can increase or decrease as one includes more or fewer points in the calculations, but the overall shapes of the curves do not change, as for the case of choosing arbitrary bins. This is particularly important in small samples and eventually under the effects of substructure. The bootstrapping method helps to characterize the confidence region. This procedure is applied in all similar statistical analyses in this work As a final visual procedure, the lines were smoothed with simple spline fits; however, this procedure, however, only erases local scale variations.

5.2. Star formation activity and environment

We investigate further the dependence of the star-formation activity on environment based on emission lines, which are sensitive to the ionizing radiation coming from the newly-formed hot stars. We plot the weighted fraction of star-forming galaxies (as defined in Sect. 2.7) and the mean of [Oıı] and Hα EWs in Fig. 9, against normalized clustercentric distance and projected density, respectively. The field value is shown as a horizontal area in the plots.

We observe that the star-formation activity is strongly suppressed in the cluster cores with less than 20% of the galaxies forming stars. This fraction increases steadily up to ~50% at $R \approx 3R_{virial}$, but it does not reach clearly the field value of ~56%. of star-forming galaxies. This field fraction is typical for those redshifts (see Hammer et al. 1997; Balogh et al. 1999; Nakata et al. 2005). Although each of these authors used different cuts to define the star-forming population, the derived values agree within the statistical uncertainties.

However, the increase in the star-formation activity with radius is irregular. In a similar way to the fraction of blue galaxies, we observe a peak at $R \sim 0.6R_{virial}$ in both, star-forming fraction and mean EWs. Only outside of $1R_{virial}$, those indicators start to increase again. The explanation for this peak is discussed in Sect. 6.2.

The mean fraction of star-forming galaxies increases linearly towards low-density regions and reaches the field value

only within the uncertainties. The mean EWs of [Oıı] and Hα follow similar trends, but they also display a peak at $\Sigma_5 \sim 60$ galaxies Mpc^{-2}. The mean EWs of those lines display similar values, which are slightly lower for [Oıı], even though that in the local universe the typical relation is $W_0([OII]) \approx 0.4W_0(H\alpha)$ (Kennicutt 1992).

The previous trends indicate that the quenching of the star-forming activity starts at slightly larger clustercentric distances and lower projected density that those sampled here.

Several studies in the local universe have found that the star-formation activity reaches the field value approximately at clustercentric distances $\sim 2R_{virial}$ and projected densities around ~ 1 galaxy Mpc^{-2}. (*e.g.* Lewis et al. 2002; Gómez et al. 2003; Rines et al. 2005). Those results are compatible with the results found here, although those low densities are not reached in this study, but the clustercentric distances are, and we still observe slight star-formation depletion at distances $R > 2R_{virial}$. As the field star-forming fraction in the local universe is much lower (~35%, see *e.g.* Rines et al. 2005), the radial trend found in this study is, therefore, steeper, indicating that the suppression of the star-formation activity in clusters at $z \sim 0.25$ was more effective, because the star-forming fraction in the internal regions of clusters is similar at all redshifts (*e.g.* Balogh et al. 1999; Nakata et al. 2005).

Pimbblet et al. (2006) studied a sample of 11 clusters between 0.07<z<0.16, with quite good coverage outside of $1R_{virial}$. Although, the results point towards similar conclusions as the studies at $z \sim 0$, the break in the star-formation activity appear to be shifted slightly towards higher densities, an effect that we cannot confirm nor exclude, although in our case the fraction approaches to the field value at $\Sigma_5 \approx 10$ galaxies Mpc^{-1}, but the differences on the density calculation hamper direct comparisons.

At higher redshifts, most studies have been focused on the central regions of clusters (*e.g.* Balogh et al. 1999, 2002a,b). Our results complement those studies, sampling similar clusters at larger clustercentric distances, with focus on the cluster-field interface. It also bridges the studies being performed by deep surveys which have focused mainly on low-density regions (*e.g.* Elbaz et al. 2007; Cooper et al. 2007; Franzetti et al. 2007).

6. Origin of the trends

To explore the origin of trends described in the previous section, we split the sample into different subsamples according to various criteria.

6.1. The star-forming population

We analyze first the properties of the star-forming population only, defined to be the galaxies with equivalent widths $W_0 > 5$ Å. The dynamical range of radius and galaxy densities is smaller because the subsample is smaller than the original sample.

The mean EWs (Fig. 10) remain stable over a wide range of clustercentric distances and density values and are statistically similar to those found for field star-forming galaxies, which imply that the populations do not differ substantially. This leads to the conclusion that the trends seen in Fig. 9 are driven only by the change in the relative numbers of star-forming and passive galaxies in different environments.

This result is similar to the findings of Balogh et al. (2004a) and Rines et al. (2005) at $z \approx 0$ who found that the mean Hα EWs display a similar distribution for star-forming galaxies located in "high" and "low" density environments.
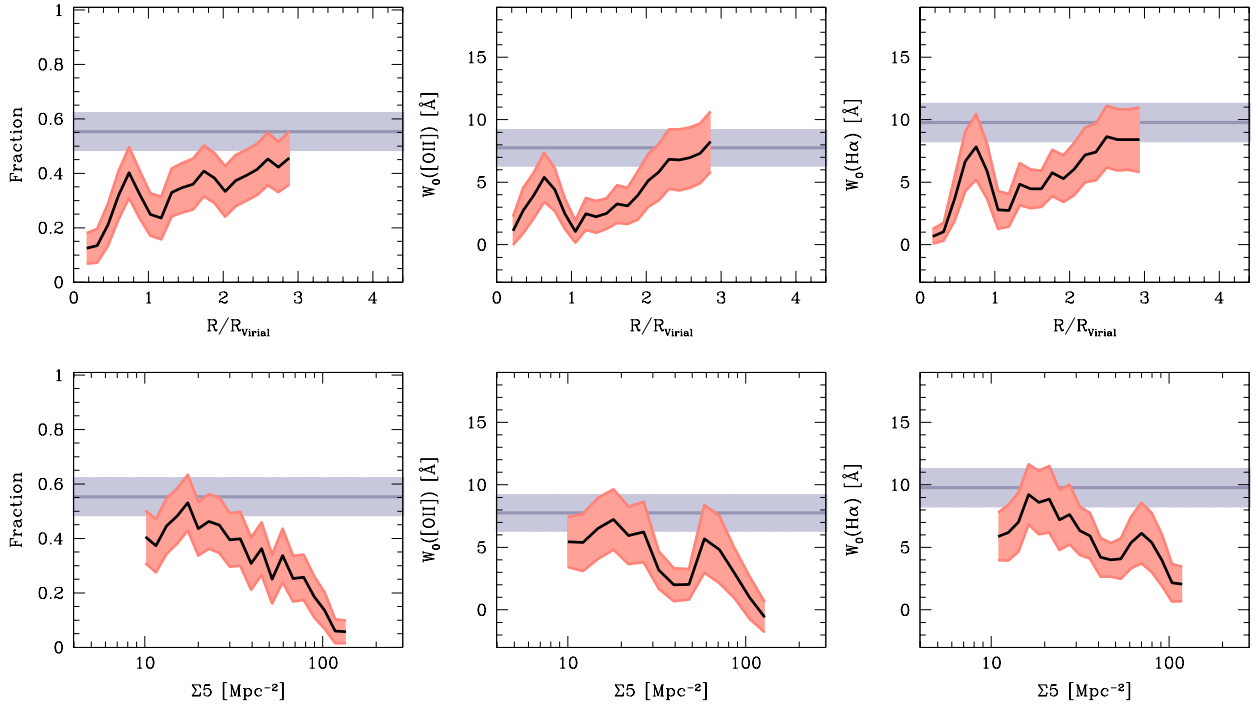
Fig. 9. Fraction of star-forming galaxies (left panels) and mean EWs of [OII] (middle panels) and Hα (right panels) against normalized clustercentric distances (top panels) and projected densities to the 5th neighbor (Σ_5, bottom panels), plotted as the thick, solid, black lines. The shaded areas around the curve in light blue are the standard deviations of the bootstrapped values. The horizontal areas show the field values for galaxies between $0.15 < z < 0.35$.
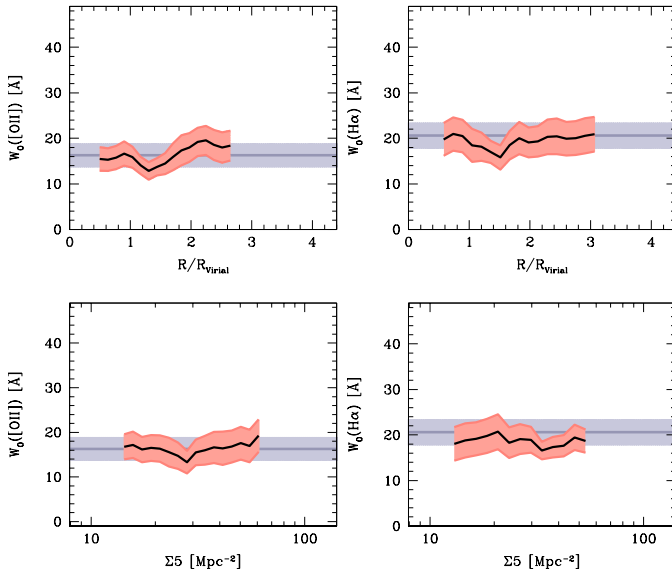
Fig. 10. Similar to figure 9 but now analyzing the distribution of the star-forming population only (*i.e.* $W_0([OII], H\alpha) > 5$Å).

This behavior of the active galaxy population, together with the strong bimodality, observed in colors (Balogh et al. 2004b) and EWs (Haines et al. 2007), detected in large local surveys favors mechanisms that trigger a rapid evolution between galaxy subtypes.

6.2. Subsamples according to membership

Given the relative small sample and some unusual features in the composite cluster, we investigate the influence of individual clusters on the final measurements for the composite cluster. Since two clusters, VMF73 and VMF131, account for an important fraction of the data used in the composite cluster, we investigate them individually. Here, given the smaller number of galaxies, we are forced to use fewer data points in our statistical analyses, which increases the level of noise.

The results can be seen in Fig. 11. We note striking differences between the clusters, especially in the radial distribution. The trends for the cluster VMF73 show peaks inside $1R_{virial}$. Therefore, we conclude that the peaks detected in the global trends are exclusively due to this cluster. The existence of this peak, or rather the depletion at $\sim 1R_{virial}$ is likely an effect of a secondary structure in this cluster (see Sect. 4.3), because the radial gradient is the combination of both substructures. This can be taken as additional evidence that the X-ray structure detected by Rasmussen & Ponman (2004) actually belongs to the cluster. It may form part of an infalling group and clearly has a noticeable effect on the galaxy population of this cluster. Additional effects may arise from the geometrical configuration of the cluster at $R < 1R_{virial}$, given its elongated galaxy concentration. Those features passed unnoticed in the previous analysis of Gerken et al. (2004) as the fixed bins used there effectively erased the detail.

VMF131 shows, on the other hand, a modest but steady increase in its star-forming activity towards larger clustercentric distances. This cluster is quite well studied at large radii. Thus, the general trends of the composite cluster at these distances are very dependent on it.
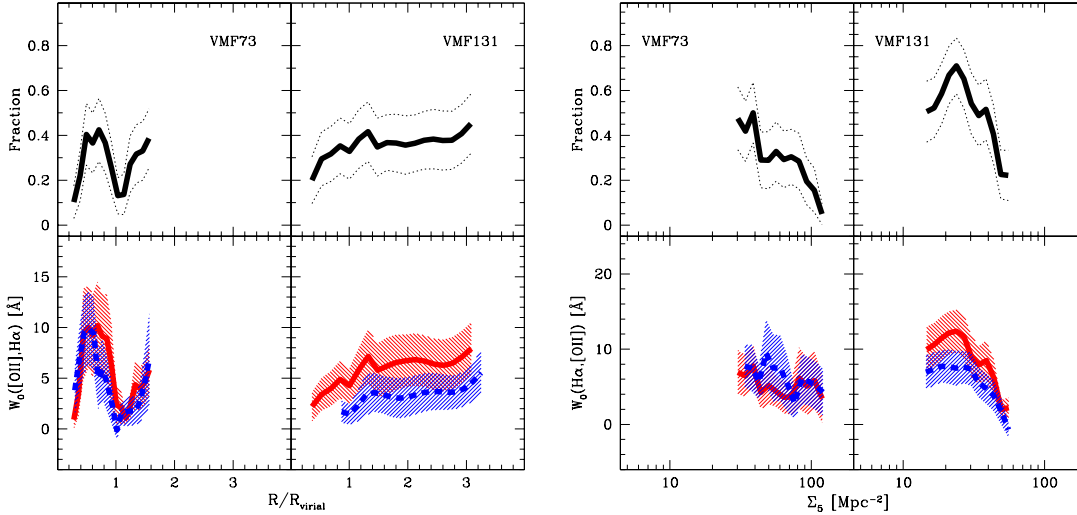
Fig. 11. Fraction of star-forming galaxies and mean equivalents widths against normalized cluster distance and projected density for the clusters VMF73 and VMF131 as depicted in the respective panels. In the bottom panels, dashed blue lines are for $\langle W_0([O_{II}])\rangle$ and solid red lines for $\langle W_0(H\alpha)\rangle$ bottom panels the dashed blue line represent the mean [O$_{II}$] EWs and the solid red line the Hα ones. The respective 1-σ are marked as the hashed areas in the bottom panels and thin dotted lines in top panels.

Since density probes environment independently of the cluster geometry, cluster substructure does not affect, in principle, the correlations. Nevertheless, we observe that the trends for these two clusters are quite different. VMF73 shows a sharp increase in the fraction of star-forming galaxies towards lower projected densities but a modest increase in their overall activity, as measured by their EWs. VMF131 displays an increase in its fraction of star-forming members and the average star-formation activity is similarly increased.

The scatter of the galaxy population inside clusters has been already noted, it does not however depend strongly on their X-ray luminosity nor velocity dispersion according to Popesso et al. (2007), although Poggianti et al. (2006) find both a weak correlation of galaxy properties with cluster mass and evolution of the correlation with redshift. This scatter may be related to more subtle properties, such as cluster substructure, mass-assembly history and intra-cluster gas distribution, as well as the properties of the large-scale structure surrounding the clusters.

7. The case of the red star-forming galaxies

We already noted in Sect. 3.2 the existence of a sub-population of cluster galaxies with emission lines but red colors. Twenty-five out of 56 star-forming galaxies belong to this population. Their average EWs are $\langle W_0([O_{II}])\rangle = 14.8 \pm 2.48$ Å and $\langle W_0(H\alpha)\rangle = 19.9 \pm 4.90$ Å, respectively, similar (within 1-σ significance levels) to the mean star-forming population (see Fig. 10). They do not seem to populate any special environment in the cluster, being more or less evenly distributed in radius and density, which explains the similarity between the blue and the star-forming fraction (Fig. 8 and 9). They also span the full range of luminosities covered by this study.

Galaxies with a red SED and star-formation activity have been routinely reported at intermediate redshifts, either in the field (*e.g.* Hammer et al. 1997) or in clusters (*e.g.* Demarco et al. 2005). In the case of the local Universe, a recent paper by Popesso et al. (2007) reports that red star-forming galaxies con-

stitute on average 25% of the entire cluster population. They suggest that those objects are in the process of evolution from late to early types. Wolf et al. (2005) identified hundreds in the field of the supercluster A901/902 ($z \approx 0.17$) based on the information content in the medium-band photometry of the COMBO-17 survey. They interpret the color of those galaxies as a product of the combination of old stellar populations and dust extinction. Similarly, Tanaka et al. (2007) presented indication of red galaxies with younger stellar populations in groups around a $z = 0.55$ cluster. They argued that those red galaxies have truncated their star formation activity recently, on a short timescale, but that they host a large fraction of old stars in a addition to a reasonable amount of dust.

On the other hand, Martini et al. (2002), based on ROSAT X-ray data, reported an unexpectedly high fraction of AGNs in elliptical galaxies in a massive $z = 0.15$ cluster, which did not show optical signatures. Although their sample is small, the fraction of obscured AGNs is similar to the fraction of blue galaxies identified in that cluster. Furthermore, Yan et al. (2006) found that more than the half of red galaxies in the SDSS-DR4 show emission lines, most of them consistent with being low ionization nuclear emission-line regions (LINERs) . However, the LINERs may not be due only to AGNs, for example Sarzi et al. (2006) report *extended* LINER-like emission in several early-type galaxies in their spatially-resolved spectroscopy. Therefore the question is not clearly settled.

To decide whether those galaxies are AGNs or not, and to what degree our star-forming galaxies may be contaminated by nuclear activity, we performed some tests based on the emission lines. We note that we may be unable to detect obscured AGNs. No galaxy shows signs of broadening typical of Seyferts 1, but Seyferts 2 and LINERs may still be present. We calculate the ratios between emission lines ([O$_{II}$], Hβ, [O$_{III}$]λ5007, Hα and [N$_{II}$]), where is possible since all lines are rarely present altogether. We conduct separate tests to check all possibilities.

The first classical test put the galaxies into the BPT plane (*i.e.* log([O$_{III}$]/Hβ) vs log([N$_{II}$]/Hα), Baldwin et al. 1981). Each par of lines are close enough to use the EWs instead of the fluxes.
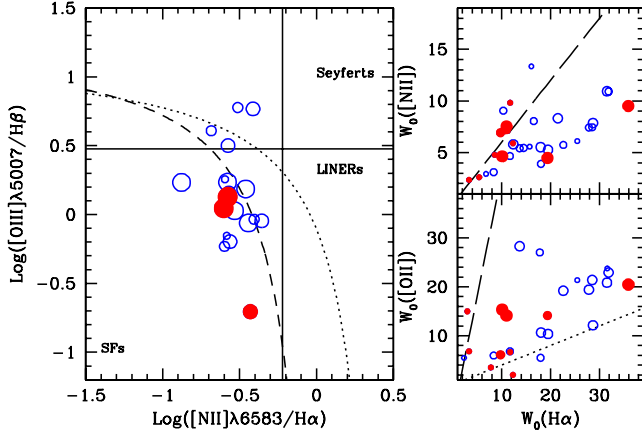
Fig. 12. Line ratio diagnostic diagrams to identify AGNs. The left panel is the BPT plane showing the relation between four emission lines. The dashed and dotted curves separate AGNs from star-forming galaxies (see text). The vertical and horizontal lines are the approximate separation between types. The lower right panel is the [OII]–Hα diagram aimed to identify LINERs. The dotted line is the local Kennicutt's relation for star-forming galaxies, whereas the dashed line is the test to identify LINERs. The upper right panel is the relation between [NII] and Hα EWs. Blue open circles are "normal" star-forming galaxies and red filled ones are the red star-forming galaxies. The size of the symbols is related to the confidence with which each index can be measured, the larger the better.

We plot in Fig. 12 all galaxies for which those indexes can be measured. The lines are the empirical separation between star-forming galaxies and AGNs of Kauffmann et al. (2003):

$$\log\left(\frac{[\text{OIII}]}{\text{H}\beta}\right) = \frac{0.61}{\log\left(\frac{[\text{NII}]}{\text{H}\alpha}\right) - 0.05} + 1.3 \qquad (2)$$

and the theoretical predictions of Kewley et al. (2001)

$$\log\left(\frac{[\text{OIII}]}{\text{H}\beta}\right) = \frac{0.61}{\log\left(\frac{[\text{NII}]}{\text{H}\alpha}\right) - 0.47} + 1.19 \qquad (3)$$

The separation between galaxy types is made using [OIII]/Hβ > 3 and [NII]/Hα > 0.6, with the latter also used independently for all galaxies where these two lines are present, which occurred more often than in the case of the four lines test.

The latest test was proposed by Yan et al. (2006). It uses only the ratio between [OII] and Hα EWs and was aimed mainly to detect LINERs.

$$W_0([\text{OII}]) > 5 \cdot W_0(\text{H}\alpha) - 7 \qquad (4)$$

In total, 10 galaxies show some signs of AGN activity with 6 being galaxies classified as "red star-forming". Note that, the emission-line data for all AGN candidates are positioned close to the boundaries of the respective tests, indicated in Fig. 12, which means that their nuclear activity is rather low or composite. The exclusion of these AGNs candidates does not affect the results shown in Fig. 9 and 10, which is an expected result because AGN frequency is not correlated with environment (Miller et al. 2003).

As noted before, in Fig. 9 and 10, the mean EWs of the [OII] and the Hα lines display similar values, even though in local samples the relation between the EWs of these emission lines follows the Kennicutt's law ($W_0([\text{OII}]) \approx 0.4W_0(\text{H}\alpha)$, Kennicutt 1992). This can be more clearly seen in the lower right corner of Fig. 12, where the Kennicutt's relation is plotted. No clear explanation has been found for this deviation, but Hammer et al. (1997) reported the same effect in the Canada-France Redshift Survey galaxies at similar redshifts. They presented various hypotheses that may apply to our work, such as, lower extinction, lower metallicities and contamination by AGNs. However, we exclude the possibility of here a strong AGN contamination and most *normal* star-forming galaxies also present these "unusual" values. The deviation is therefore probably caused by the lower metallicities present in distant galaxies (see Kobulnicky & Kewley 2004), because the [OII]-Hα ratio depends strongly on this parameter (Jansen et al. 2001).

We can estimate the contribution of dust extinction using the Tully & Fouque (1985) extinction laws for disk galaxies. At $z \approx 0.25$, the V and I filters correspond approximately to restframe B and R-bands. At a given inclination angle, the extinction in the R-band is $\sim 0.56E(B)$: only disk galaxies with inclinations larger than $60°$ will therefore have a correction factor $E(B-R) > 0.2$ mag (see Table 1 in Böhm et al. 2004), a value sufficiently large to move their data-points away from red-sequence.

Our *ground-based* INT images do not allow us to securely classify the morphological properties of our galaxies, since the typical seeing of ~ 1 arcsec (~ 4 kpc at $z = 0.25$) represents approximately one scale-length for spiral galaxies (*e.g.* Bamford et al. 2007). Basic properties can however be obtained, as galaxies in our sample typically have an apparent size of 5–10 arcsec. After examination, we find that out of the 25 "red star-forming" galaxies, 11 are clearly spirals, 11 appear bulge-dominated, two are irregular and one galaxy, which is also an AGN candidate, shows signs of interaction. Out of 11 spirals, 8 are probably edge-on galaxies and the remaining three, face-on.

Dust extinction can, therefore, explain the colors of only a fraction of the red star-forming objects, because dust properties at $z \sim 0.25$ do not differ much from those of the local universe, and highly-tilted galaxies can be easily distinguished.

The red star-forming galaxies appear to be transition objects populating the "green valley" (Salim et al. 2007) in Fig. 13, where we plot the specific star-formation (sSFR) activity[5] versus stellar mass. Most of the red-star forming galaxies (as well as some AGNs) are located in a "transition region" between normal star-forming galaxies and passive ones[6]. The mean sSFR for normal star-forming galaxies is $\sim (1.08 \pm 0.65) \times 10^{-10}$ yr^{-1}, whereas the red star-forming galaxies have on average $sSFR \approx (2.4 \pm 0.6) \times 10^{-11}$ yr^{-1}, about an order of magnitude lower. The average upper limit for passive galaxies is $sSFR \approx (4.8 \pm 3.3) \times 10^{-12}$ yr^{-1} because we do not include galaxies with unphysical star-formation rates.

We note that those galaxies may also be present in the field, although we cannot clearly identify them, given the uncertainties in the k-corrections of ~ 0.2 mag, which are larger than typical red-sequence scatter. However, it can be seen that most of the normal field and cluster star-forming galaxies are located in the upper part of this diagram, around the relation for local galaxies found in the UV-selected sample of Salim et al. (2007). We note

---

[5] The derivation of the sSFRs is described in Appendix A.

[6] Here galaxies with $5 > W_0([\text{OII}], \text{H}\alpha) > 0$ are also plotted. Galaxies with negative EWs were not used since the calculations yield unphysical (*i.e.* negative values) results.
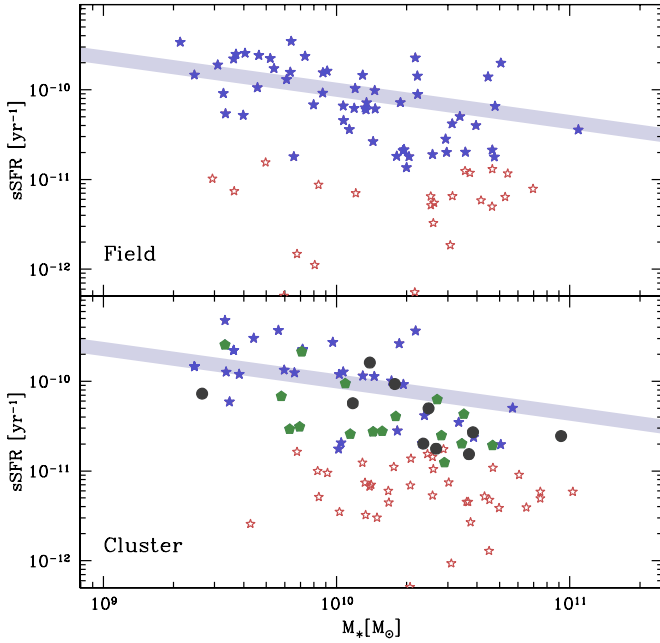
Fig. 13. Specific star formation rates for field (top) and cluster (bottom) galaxies, versus stellar mass. Normal star-forming galaxies are plotted with blue filled stars and the red star-forming galaxies with green pentagons. The red open stars are passive galaxies with $0 < W_0([\text{O\textsc{ii}}], \text{H}\alpha) < 5$ and are shown for comparison. The black circles are the AGN candidates. The thick line is the local relation from Salim et al. 2007.

that field and cluster star-forming galaxies are located in similar regions of this diagram, an additional indication that both populations are composed similar classes of objects. However, the red star-forming galaxies appear to be clearly offset from this relation.

It is interesting to note that the definition of a star-forming galaxy set at $W_0([\text{O\textsc{ii}}], \text{H}\alpha) \geq 5$ Å not only has a observational sense but also a physical meaning and corresponds to a $sSFR \approx 2 \times 10^{-11}$ yr^{-1}, a rate sufficiently low to consider a galaxy as passive.

It is part of the standard picture of galaxy evolution that objects in the blue cloud (here the star-forming sequence) slowly grow in stellar mass via gas accretion over cosmic times. Mergers and other strong interactions can trigger star-bursts, displacing upwards the galaxies in the diagram (Fig. 13) adding a large amount of stellar mass in a short period of time (so moving rightwards). On the other hand, gas exhaustion or gas removal by means of interactions or feedback processes can lead to a quenching of star-formation that moves the galaxy downwards, towards the red sequence, where it can experience small episodes of star-formation, accrete more gas and move again into the blue cloud, or stay permanently there if the environment is hostile (as in the galaxy clusters cores).

In this picture, the red star-forming galaxies are located in an intermediate stage between the two main subtypes, with lower but still appreciable amounts of star-formation. The variation in the abundance of this population with cosmic time may provide additional insights into the nature of the stellar mass buildup, although, a more careful treatment of AGN activity, dust extinction and stellar population is required to fully explain their nature.

8. Summary and conclusions

We have obtained MOSCA spectroscopy for 149 member galaxies in 6 clusters at $\langle z \rangle \sim 0.25$, out to large clustercentric distances. This sample is compared directly with 97 galaxies in the field. The spectroscopic dataset is complemented with V and I-band photometry in the three fields and multiband photometry from the SDSS in two of them. The main findings can be summarized in the following.

1. The suppression of the star-formation activity can be detected at large clustercentric distances ($R > 1R_{virial}$) and low densities $\Sigma_5 < 10$ Mpc^{-1}, in an environment where the cluster is supposed to have little influence. This result agrees with similar results at redshift $z \approx 0$ based on the 2dF Galaxy Redshift Survey (Lewis et al. 2002) or SDSS (Gómez et al. 2003), where a critical value of density was found, below which the environment appear to begin to play a critical role. Although our density estimates are not directly comparable to these low-redshift studies, it is possible that we did not reach this low threshold of $\Sigma_5 \sim 1$Mpc^{-2} reported by those studies. Our investigation reached star-formation activities close to those found in the field, probing the transition between field and cluster environment in the distant Universe. The decrease of the star-formation activity is smooth with increasing density, but a more complex behavior was found when the radial dependence is studied, as it is strongly affected by substructure.

2. The trends in the star-formation activity measured by the mean [O\textsc{ii}] and Hα EWs are due mainly to a strong decrease in the relative number of star-forming galaxies towards higher densities and smaller clustercentric distances, rather than a slow decline in the star-formation rates of galaxies. This finding favors violent suppression of the star-formation activity.

3. Despite the importance of the overall trends, important differences are found between the studied clusters. The two most well-studied clusters were analyzed separately from all other clusters.. It was found that the shape of the star-formation gradients were quite different from each other.. This difference was more accentuated in the radial trends since the effects of substructure could not be discerned in the assumed radial density profile.
In the literature, many studies have focused either solely on one usually well-sampled cluster (*e.g.* Kodama et al. 2001; Demarco et al. 2005; Sato & Martin 2006), or on a family of clusters (selected by X-ray luminosity, redshift range, etc), generally far less well-sampled, which typically combine all data to create a "composite-cluster" (*e.g.* Balogh et al. 1999, 2002a; Pimbblet et al. 2006) in a similar way to our analysis here. However, our study indicates that many of the overall trends may not be universal, but may be strongly related to the particularities of the system that the individual galaxies belong to. Therefore, the effects of the substructure should not be neglected when analyzing the universality of star-formation-environment relation, because each particular system may have different properties (see also Rines et al. 2005 for a similar result at $z = 0$).

4. The clusters show variations not only due to the substructure, but also in their galaxy populations. For example, we detected an important sub-population of red star-forming galaxies in some clusters, which have similar colors or are redder than the red-sequence. The characteristics of this population, as measured by their environmental distribution, do not differ much from the remainder of the emission-line pop-

ulation. A fraction of them could be AGNs, but the AGN contamination is not larger than in the rest of the star-forming population. Nonetheless, all AGN candidates show relatively low activity.

Dust may play a role because some galaxies are clearly edge-on spirals. This effect may be o present in other galaxies. It is, however, intriguing that some otherwise blue active star-forming galaxies have the precise amount of dust to make them fall onto the narrow red sequence.

These two effects together, however, are only able to explain a fraction of this population.

These galaxies are located in a transition zone, between normal star-forming galaxies and passive ones, where galaxies appear to form stars at a relatively lower rate. They may be in the process of shutting down their activity and/or they can contain a relatively significant old stellar population combined with a moderate amount of dust. If these galaxies are truly transition objects, their abundance may provide important clues about the mass-assembly history as galaxies grow in mass via accretion and merging and shut down their star-formation over cosmic time (*e.g.* Bell et al. 2005).

Our results favor mechanisms of strong star-formation suppression. Among the preferred processes is ram-pressure stripping (and other strong galaxy interactions within the intracluster medium). This process can quench the star-formation on timescale as short as 1 Gyr, which is the dynamical timescale of a cluster passage. Ram-pressure is very effective in the central regions of the clusters (*e.g.* Kapferer et al. 2007). We detect however star-formation depletion at clustercentric distances as far as $\sim 3R_{virial}$. It is possible that many galaxies in the outskirts have already passed through the denser intracluster media. In fact, models by Gill et al. (2005) predict that as many as half of the galaxies between $1–2.5R_{virial}$ may be "bouncing" after a first passage (the "backsplash" scenario) and thus have experienced strong interactions in the inner cluster core for a sufficient time to explain their passive nature. Therefore, ram-pressure stripping cannot disregarded as a important mechanism, particularly because, since direct evidence of this process at work has been reported by some authors (*e.g.* Boselli et al. 2006; Cortese et al. 2007).

Other processes may be still acting, because quenching of star-formation is observed at distances larger than those predicted by the Gill et al. (2005) simulations. Also, their proposed "backsplash" population would only account for a fraction of the galaxy population in the cluster outskirts. Any other process that quenches that star-formation more gradually (*e.g.* starvation, harassment, etc) would have been detected via enhancement or depletion in the star-forming population with environment, which is not the case. One possibility is that other processes affect the star-formation on galaxies before they begin to fall into the clusters, in groups and filaments embedded in the large-scale structure. In those environments, several processes are thought to be effective in changing the galaxy stellar populations. Ram-pressure stripping may still be effective in systems of lower masses under certain certain conditions (*e.g.* Fujita 2004; Hester 2006) and thus may contribute. Merger and tidal interactions in those environments are also likely and they can trigger starbursts that consume gas rapidly and strip the remaining gas via feedback mechanisms(*e.g.* Bekki 2001; Fujita 2004). This scenario is compatible with the recent findings of Tanaka et al. (2007) and Haines et al. (2007).

It is important to note that every cluster is a particular entity of its own and it is likely that different processes are important. They can depend on the cluster history and configuration, as well as on the characteristics of the surrounding environment. These effects may influence the galaxy population that inhabit the clusters as shown recently by Moran et al. (2007). This view is supported here by the different star-formation gradients detected, due mainly to substructure and the abundances in the galaxy population, with some clusters harboring an important fraction of red-star forming galaxies, which may be important in the general scheme of galaxy evolution.

References

Baldwin, J. A., Phillips, M. M., & Terlevich, R. 1981, PASP, 93, 5
Balogh, M., Bower, R. G., Smail, I., et al. 2002a, MNRAS, 337, 256
Balogh, M., Eke, V., Miller, C., et al. 2004a, MNRAS, 348, 1355
Balogh, M. L., Baldry, I. K., Nichol, R., et al. 2004b, ApJ, 615, L101
Balogh, M. L., Morris, S. L., Yee, H. K. C., Carlberg, R. G., & Ellingson, E. 1999, ApJ, 527, 54
Balogh, M. L., Smail, I., Bower, R. G., et al. 2002b, ApJ, 566, 123
Bamford, S. P., Milvang-Jensen, B., & Aragón-Salamanca, A. 2007, MNRAS, 378, L6
Beers, T. C., Flynn, K., & Gebhardt, K. 1990, AJ, 100, 32
Bekki, K. 2001, ApJ, 546, 189
Bekki, K., Couch, W. J., & Shioya, Y. 2002, ApJ, 577, 651
Bell, E. F., Papovich, C., Wolf, C., et al. 2005, ApJ, 625, 23
Blanton, M. R., Dalcanton, J., Eisenstein, D., et al. 2001, AJ, 121, 2358
Blanton, M. R., Eisenstein, D., Hogg, D. W., Schlegel, D. J., & Brinkmann, J. 2005, ApJ, 629, 143
Blanton, M. R. & Roweis, S. 2007, AJ, 133, 734
Böhm, A., Ziegler, B. L., Saglia, R. P., et al. 2004, A&A, 420, 97
Boselli, A., Boissier, S., Cortese, L., et al. 2006, ApJ, 651, 811
Bower, R. G. 1991, MNRAS, 248, 332
Bruzual, G. & Charlot, S. 2003, MNRAS, 344, 1000
Butcher, H. & Oemler, Jr., A. 1978, ApJ, 226, 559
Carlberg, R. G., Yee, H. K. C., & Ellingson, E. 1997, ApJ, 478, 462
Cooper, M. C., Newman, J. A., Weiner, B. J., et al. 2007, ArXiv e-prints, 706
Cortese, L., Marcillac, D., Richard, J., et al. 2007, MNRAS, 376, 157
David, L. P., Slyz, A., Jones, C., et al. 1993, ApJ, 412, 479
Demarco, R., Rosati, P., Lidman, C., et al. 2005, A&A, 432, 381
Dressler, A. 1980, ApJ, 236, 351
Dressler, A., Oemler, A. J., Couch, W. J., et al. 1997, ApJ, 490, 577
Elbaz, D., Daddi, E., Le Borgne, D., et al. 2007, A&A, 468, 33
Ellingson, E., Lin, H., Yee, H. K. C., & Carlberg, R. G. 2001, ApJ, 547, 609
Franzetti, P., Scodeggio, M., Garilli, B., et al. 2007, A&A, 465, 711
Fujita, Y. 2004, PASJ, 56, 29
Fukugita, M., Shimasaku, K., & Ichikawa, T. 1995, PASP, 107, 945
Gehrels, N. 1986, ApJ, 303, 336
Gerken, B., Ziegler, B., Balogh, M., et al. 2004, A&A, 421, 59
Gilbank, D. G., Bower, R. G., Castander, F. J., & Ziegler, B. L. 2004, MNRAS, 348, 551
Gill, S. P. D., Knebe, A., & Gibson, B. K. 2005, MNRAS, 356, 1327
Gnedin, O. Y. 2003, ApJ, 589, 752
Gómez, P. L., Nichol, R. C., Miller, C. J., et al. 2003, ApJ, 584, 210
Goto, T., Yamauchi, C., Fujita, Y., et al. 2003, MNRAS, 346, 601
Haines, C. P., Gargiulo, A., La Barbera, F., et al. 2007, MNRAS, 381, 7
Hammer, F., Flores, H., Lilly, S. J., et al. 1997, ApJ, 481, 49
Harker, J. J., Schiavon, R. P., Weiner, B. J., & Faber, S. M. 2006, ApJ, 647, L103
Hernquist, L. 1992, ApJ, 400, 460
Hester, J. A. 2006, ApJ, 647, 910
Hicks, A. K., Ellingson, E., Hoekstra, H., & Yee, H. K. C. 2006, ApJ, 652, 232
Hogg, D. W., Blanton, M. R., Eisenstein, D. J., et al. 2003, ApJ, 585, L5
Hopkins, A. M. 2004, ApJ, 615, 209
Hubble, E. P. 1936, Yale University Press
Jansen, R. A., Franx, M., & Fabricant, D. 2001, ApJ, 551, 825
Kapferer, W., Kronberger, T., Weratschnig, J., et al. 2007, A&A, 466, 813
Kauffmann, G. 1996, MNRAS, 281, 487

Kauffmann, G., Heckman, T. M., Tremonti, C., et al. 2003, MNRAS, 346, 1055
Kennicutt, Jr., R. C. 1992, ApJ, 388, 310
Kewley, L. J., Dopita, M. A., Sutherland, R. S., Heisler, C. A., & Trevena, J. 2001, ApJ, 556, 121
Kobulnicky, H. A. & Kewley, L. J. 2004, ApJ, 617, 240
Kodama, T. & Bower, R. G. 2001, MNRAS, 321, 18
Kodama, T., Smail, I., Nakata, F., Okamura, S., & Bower, R. G. 2001, ApJ, 562, L9
Larson, R. B. & Tinsley, B. M. 1978, ApJ, 219, 46
Lewis, I., Balogh, M., De Propris, R., et al. 2002, MNRAS, 334, 673
Markevitch, M. 1998, ApJ, 504, 27
Martini, P., Kelson, D. D., Mulchaey, J. S., & Trager, S. C. 2002, ApJ, 576, L109
Mason, K. O., Carrera, F. J., Hasinger, G., et al. 2000, MNRAS, 311, 456
Miller, C. J., Nichol, R. C., Gómez, P. L., Hopkins, A. M., & Bernardi, M. 2003, ApJ, 597, 142
Moore, B., Lake, G., & Katz, N. 1998, ApJ, 495, 139
Moran, S. M., Ellis, R. S., Treu, T., et al. 2007, ApJ, 671, 1503
Moustakas, J., Kennicutt, Jr., R. C., & Tremonti, C. A. 2006, ApJ, 642, 775
Mullis, C. R., McNamara, B. R., Quintana, H., et al. 2003, ApJ, 594, 154
Nakata, F., Bower, R. G., Balogh, M. L., & Wilman, D. J. 2005, MNRAS, 357, 679
Pimbblet, K. A., Smail, I., Edge, A. C., et al. 2006, MNRAS, 366, 645
Poggianti, B. M., von der Linden, A., De Lucia, G., et al. 2006, ApJ, 642, 188
Popesso, P., Biviano, A., Romaniello, M., & Böhringer, H. 2007, A&A, 461, 411
Quilis, V., Moore, B., & Bower, R. 2000, Science, 288, 1617
Rasmussen, J. & Ponman, T. J. 2004, MNRAS, 349, 722
Rines, K., Geller, M. J., Kurtz, M. J., & Diaferio, A. 2003, AJ, 126, 2152
Rines, K., Geller, M. J., Kurtz, M. J., & Diaferio, A. 2005, AJ, 130, 1482
Salim, S., Rich, R. M., Charlot, S., et al. 2007, ApJS, 173, 267
Sarzi, M., Falcón-Barroso, J., Davies, R. L., et al. 2006, MNRAS, 366, 1151
Sato, T. & Martin, C. L. 2006, ApJ, 647, 934
Schlegel, D. J., Finkbeiner, D. P., & Davis, M. 1998, ApJ, 500, 525
Tanaka, M., Hoshi, T., Kodama, T., & Kashikawa, N. 2007, MNRAS, 379, 1546
Tanaka, M., Kodama, T., Arimoto, N., et al. 2005, MNRAS, 362, 268
Toomre, A., Tinsley, B., & Larson, R. 1977, The Evolution of Galaxies and Stellar Populations, 401
Tully, R. B. & Fouque, P. 1985, ApJS, 58, 67
Vikhlinin, A., McNamara, B. R., Forman, W., et al. 1998, ApJ, 502, 558
Wolf, C., Gray, M. E., & Meisenheimer, K. 2005, A&A, 443, 435
Xue, Y.-J. & Wu, X.-P. 2000, ApJ, 538, 65
Yan, R., Newman, J. A., Faber, S. M., et al. 2006, ApJ, 648, 281
York, D. G., Adelman, J., Anderson, Jr., J. E., et al. 2000, AJ, 120, 1579

Appendix A: Star formation rates

All indicators of star-formation rates (SFRs) have their own bias and systematics due to the different processes traced for each of them (for a recent review see Moustakas et al. 2006). In the optical, at least two effects are very important: extinction and metallicity. On the other hand, optical SFRs calculation requires accurate flux calibration, that we lack. However we can still estimate SFRs using the EWs and the absolute magnitudes (calculated in Sect. 2.8) as a proxy of the continuum flux. Fortunately, our spectra cover both [OII] and Hα lines, so both results can be compared.

For [OII] derived SFRs, we can take the calibrated relation of Kennicutt (1992)

$$SFR([\text{OII}]) = 3.4 \times 10^{-12} \left(\frac{L_B}{L_{B,\odot}} \right) W_0([\text{OII}]) E(\text{H}\alpha) \ [\text{M}_\odot \ \text{yr}^{-1}] \quad \text{(A.1)}$$

where $E(\text{H}\alpha)$ is the extinction at Hα, which according to the same paper is approximately 1 mag, and $(L_B/L_{B,\odot}) = 10^{0.4(M_B - M_{B,\odot})}$, with $M_{B,\odot} = 5.48$ mag.

For Hα, we also take the relation given by Kennicutt (1992):

$$SFR(\text{H}\alpha) = 7.9 * 10^{-42} L(\text{H}\alpha) E(\text{H}\alpha) \quad \text{(A.2)}$$
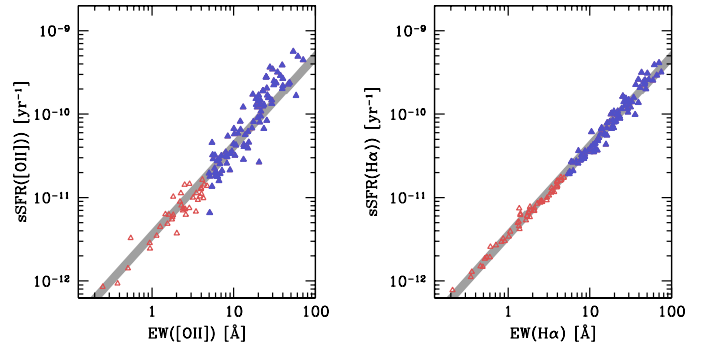
Fig. A.1. Specific star formation rates based on [OII] and Hα respectively calculated using the relations indicated in the text. Blue filled triangles are galaxies with $W_0([\text{OII}], \text{H}\alpha) > 5$ Å, classified here as star forming. The thick line is the fit to the Hα relation: $\log(sSFR) \approx 1.07 \log(W_0(\text{H}\alpha)) - 11.4$, which is plotted in the [OII] panel for comparison. Note that the sSFR obtained with the [OII] line may be slightly overestimated.

with $E(\text{H}\alpha) = 1$ mag, as indicated above. However, we do not have Hα fluxes, but we can estimate it from our R-band absolute magnitudes and Hα EWs, since

$$W_0(\text{H}\alpha) \approx \frac{L(\text{H}\alpha)}{L_C} \quad \text{(A.3)}$$

where L_C is the continuum luminosity in erg s^{-1}Å^{-1} (see Lewis et al. 2002) and $L_C \approx L_R$. For a $L^\star$ galaxy, $L_C = 1.1 \times 10^{40}$ ergs s^{-1}, as determined by Blanton et al. (2001), with $M_R^\star = -21.8$ mag, leaving:

$$L(\text{H}\alpha) = 1.1 \times 10^{40} W_0(\text{H}\alpha) 10^{-0.4(M_R - M_R^\star)} \ [\text{ergs s}^{-1}]. \quad \text{(A.4)}$$

Therefore, finally we have

$$SFR(\text{H}\alpha) = 0.079 W_0(\text{H}\alpha) 10^{-0.4(M_R + 21.8)} \ [\text{ergs s}^{-1}]. \quad \text{(A.5)}$$

We obtained SFRs for all galaxies in which either of these two lines is measurable. Both ways are likely to have systematics and uncertainties, [OII] because it is a calibrated relation and doubts persist about its universality (*e.g.* Hammer et al. 1997). Also it is strongly affected by dust and metallicity. In the case of Hα, the assumptions here made, introduce uncertainties about the accuracy of the flux. Therefore, we take the average of the SFR obtained from [OII] and Hα and when only one line is present we take this value. We did obtain SFRs for galaxies considered passive, however those values probably have larger uncertainties, so their SFRs can be considered as an upper limit . We always make distinction of both populations based in the EW distinction (see Sect. 2.7). We did not attempt to obtain SFRs for galaxies with negative equivalent widths because they yield to unphysical values, difficult to interprete if included.

Using the stellar masses obtained with KCORRECT (see Sect. 2.8) we obtained the specific star formation rates (sSFR). It is remarkable the strong correlation with little scatter between EWs and sSFR, obtained in either way (*i.e.* [OII] and Hα) and the little scatter (albeit larger for [OII]), as well as the similar values displayed using both methods (see Fig. A.1), despite the rough estimation made here. Also, it is important that both indicators yield similar values as the Hα line becomes inaccessible at larger redshifts and only [OII] can be used.

Online Material

Table 3. Data for individual objects. We only present galaxies for which we obtained *secured* redshifts (see section 2.4). Note that we include *all* objects for which we were able to obtain the following parameters. Many objects were excluded in the analysis in order to obtain a homogeneous sample (see sections 3.5 & 4.4). The columns are the following. Column (1): Object ID. Column (2): cluster, group or field membership. Columns (3) and (4): J2000 sky coordinates. Column (6): redshift. Column (7): The *I*-band magnitude. Column (8): The $V-I$ color. Columns (8) and (9): The absolute magnitudes in the restframe *B* and *R*-bands. Column (10): The logarithm of the stellar mass. Columns (11) and (12): The [OII] EWs and errors. Columns (13) and (14): The Hα EWs and errors.

(1) ID	(2) membership	(3) RA	(4) DEC	(5) z	(6) I [mag]	(7) V-I [mag]	(8) M_B [mag]	(9) M_R [mag]	(10) log(M_*) [$M_\odot$]	(11) [OII] [Å]	(12) E([OII]) [Å]	(13) Hα [Å]	(14) E(Hα) [Å]
r2211_07	vmf194	17:29:15.26	74:41:23.8	0.20998	18.59	1.388	-19.63	-20.94	10.02	9.66	0.75	0.75	0.23
r2211_08	vmf194	17:29:19.77	74:41:11.2	0.21167	16.75	1.426	-21.42	-22.79	10.78	8.95	0.95	1.10	0.23
r2211_09	vmf194	17:29:22.67	74:40:39.6	0.21187	18.17	1.462	-19.96	-21.37	10.22	0.43	0.48	-1.71	0.19
r2211_10	vmf194	17:29:30.06	74:40:43.0	0.21107	18.54	1.422	-19.64	-21.01	10.06	0.18	0.55	1.13	0.24
r2212_06	vmf194	17:29:13.37	74:42:13.8	0.20875	18.71	0.998	-19.96	-20.84	9.85	-32.93	0.63	-41.10	0.85
r2212_08	vmf194	17:29:22.55	74:40:52.3	0.21080	17.92	1.409	-20.27	-21.62	10.30	3.93	0.60	1.12	0.28
r2212_23	vmf194	17:30:44.85	74:39:11.8	0.20984	18.34	1.387	-19.87	-21.18	10.12	8.32	2.22	-0.87	0.36
r2221_14	vmf194	17:26:24.27	74:27:35.2	0.20877	17.66	1.321	-20.62	-21.85	10.37	-0.02	0.69	-10.33	0.30
r2221_03	xdcs220	17:26:50.67	74:34:04.6	0.26591	18.30	1.001	-20.92	-21.86	10.26	-39.80	0.67	-52.51	0.87
r2221_03b	xdcs220	17:26:50.87	74:34:08.8	0.26652	19.52	0.880	-19.83	-20.66	9.75	-61.16	1.72	-45.71	1.66
r2221_12	xdcs220	17:26:11.11	74:28:26.6	0.26227	18.24	1.429	-20.52	-21.89	10.41	-4.34	0.85	1.46	0.61
r2222_03	xdcs220	17:26:17.74	74:34:09.3	0.25712	18.85	1.587	-19.68	-21.19	10.17	0.21	0.39	-0.91	0.17
r2222_07	xdcs220	17:26:33.92	74:31:55.8	0.26087	19.20	1.419	-19.56	-20.90	10.02	3.07	0.41	0.76	0.24
r2231_05	xdcs220	17:24:11.04	74:31:12.1	0.26144	18.58	1.441	-20.16	-21.52	10.27	4.80	0.35	3.06	0.23
r2241_05	xdcs220	17:23:24.91	74:44:42.8	0.26168	18.39	1.592	-20.20	-21.71	10.38	-0.02	1.23	3.42	0.52
r2241_07	xdcs220	17:23:28.45	74:43:41.7	0.25977	17.00	1.572	-21.59	-23.09	10.92	5.64	0.45	1.65	0.17
r2241_09	xdcs220	17:23:26.66	74:43:16.6	0.25991	16.93	1.592	-21.64	-23.16	10.96	-14.98	0.51	-3.00	0.20
r2241_10	xdcs220	17:23:24.29	74:42:56.2	0.25953	17.99	1.518	-20.64	-22.10	10.52	8.83	0.64	2.30	0.20
r2241_15	xdcs220	17:23:32.26	74:40:35.7	0.25489	18.46	1.241	-20.43	-21.61	10.26	-1.46	0.43	-12.41	0.24
r2241_18	xdcs220	17:23:05.48	74:39:30.5	0.25451	18.38	2.567	-19.55	-21.63	10.43	-20.46	0.29	-35.91	0.28
r2242_06	xdcs220	17:23:26.46	74:43:57.3	0.26169	19.49	1.465	-19.23	-20.63	9.91	-3.18	1.04	7.17	0.62
r2251_04	xdcs220	17:24:12.22	74:22:23.8	0.26246	18.92	0.879	-20.37	-21.24	9.98	-37.27	1.09	-47.44	0.77
xdc29_04	xdcs220	17:23:29.37	74:43:38.7	0.26160	17.96	0.870	-20.63	-22.15	10.55	0.72	0.58	-1.36	0.31
r2621_14	vmf131	13:11:22.18	32:28:53.8	0.29902	19.24	1.613	-19.75	-21.26	10.19	0.98	0.30	0.35	0.20
r2621_15	vmf131	13:11:23.60	32:28:56.3	0.29347	18.95	1.079	-20.44	-21.49	10.16	-23.51	0.17	-21.69	0.23
r2621_16	vmf131	13:11:24.66	32:28:36.9	0.30015	18.99	1.340	-20.24	-21.50	10.23	-20.84	0.24	-31.54	0.33
r2631_20	vmf131	13:10:41.55	32:28:23.1	0.29691	17.24	1.777	-21.58	-23.23	11.01	2.72	0.48	-1.85	0.34
r2632_02	vmf131	13:10:16.57	32:30:36.6	0.29501	18.70	1.719	-20.14	-21.75	10.41	2.09	0.23	-1.66	0.16
r2632_02b	vmf131	13:10:16.86	32:30:38.0	0.29341	19.92	1.087	-19.46	-20.52	9.77	-22.93	0.46	-31.87	0.78
r2632_03	vmf131	13:10:18.96	32:30:18.7	0.29380	18.47	1.693	-20.38	-21.97	10.49	-0.38	0.18	0.15	0.13
r2632_11	vmf131	13:10:30.42	32:27:16.6	0.29477	17.73	1.508	-21.29	-22.71	10.75	-10.37	0.15	-19.49	0.16
r2632_12	vmf131	13:10:34.20	32:27:30.8	0.29464	19.21	1.024	-20.25	-21.22	10.02	-19.41	0.21	-27.83	0.33
r2632_17	vmf131	13:10:47.14	32:27:56.8	0.29270	19.37	1.586	-19.57	-21.06	10.11	-4.03	0.30	-3.99	0.20
r2641_04	vmf131	13:10:17.22	32:19:51.8	0.29577	18.90	1.903	-19.78	-21.56	10.36	-2.01	1.15	-12.32	0.90
r2641_05	vmf131	13:10:14.02	32:23:33.6	0.29617	18.71	1.774	-20.10	-21.75	10.42	-0.16	1.23	-11.21	0.91
r2641_06	vmf131	13:10:12.94	32:24:09.1	0.29574	18.59	0.864	-21.02	-21.84	10.21	2.78	0.52	1.22	0.30
r2641_07	vmf131	13:10:10.66	32:21:44.2	0.29329	18.77	2.331	-19.59	-21.67	10.45	-5.09	0.38	-15.73	0.35
r2641_12	vmf131	13:10:01.42	32:23:48.2	0.29614	17.98	1.500	-21.07	-22.47	10.65	....	....	-0.36	0.39
r2651_08	vmf131	13:10:47.60	32:20:11.4	0.29430	18.48	1.632	-20.43	-21.96	10.48	-2.87	0.25	2.55	0.18
r2651_17	vmf131	13:11:13.98	32:19:10.5	0.29438	17.54	1.744	-21.27	-22.90	10.87	-4.27	0.17	-0.60	0.11
r2651_19	vmf131	13:11:17.96	32:19:47.9	0.29408	18.15	1.511	-20.86	-22.28	10.58	-5.96	0.22	-8.38	0.15
ba_07	vmf131	13:10:05.72	32:21:12.2	0.29651	18.32	1.105	-21.08	-22.13	10.42	5.07	0.80	0.24	0.60
ba_09	vmf131	13:10:04.22	32:21:36.3	0.29003	19.00	1.615	-19.89	-21.39	10.25	3.28	0.81	2.95	0.70
ba_12	vmf131	13:09:55.05	32:21:49.0	0.29382	18.47	1.684	-20.39	-21.97	10.49	3.51	0.55	3.18	0.36
ba_14	vmf131	13:09:53.20	32:21:59.8	0.29125	18.87	1.681	-19.97	-21.53	10.31	4.67	0.68	-2.11	0.43
ba_18	vmf131	13:10:11.38	32:22:02.3	0.29388	18.15	1.666	-20.74	-22.29	10.61	6.15	0.49	0.20	0.35
ba_25	vmf131	13:09:51.54	32:22:17.8	0.29242	18.40	1.689	-20.45	-22.02	10.51	5.13	0.50	0.13	0.35
ba_28	vmf131	13:09:56.11	32:22:16.8	0.29207	16.72	1.718	-22.10	-23.70	11.18	5.12	0.35	0.84	0.22
ba_30	vmf131	13:09:58.50	32:22:31.3	0.29466	18.02	1.670	-20.86	-22.42	10.67	2.29	0.48	1.07	0.34
ba_36	vmf131	13:10:00.18	32:22:59.4	0.29431	18.23	1.361	-20.93	-22.21	10.52	-6.82	0.38	-11.69	0.35
ba_37	vmf131	13:09:56.33	32:23:10.8	0.28946	18.21	1.701	-20.60	-22.19	10.58	-6.66	0.77	-11.75	0.59
ba_39	vmf131	13:09:57.68	32:23:13.0	0.29233	17.95	1.708	-20.88	-22.47	10.69	-2.66	0.46	-0.46	0.31
r2611_04	vmf132	13:12:07.22	32:34:35.8	0.24552	18.99	1.422	-19.61	-20.95	10.04	6.99	0.54	2.91	0.32
r2611_13	vmf132	13:11:51.74	32:33:29.2	0.24964	17.79	1.463	-20.81	-22.20	10.54	6.78	0.35	1.40	0.21
r2611_14	vmf132	13:11:49.17	32:33:23.4	0.24656	18.11	1.488	-20.42	-21.85	10.41	0.91	0.40	1.31	0.23
r2612_02	vmf132	13:12:27.01	32:32:06.6	0.24855	18.53	1.497	-20.01	-21.44	10.25	-15.32	0.23	-10.12	0.13
r2612_04	vmf132	13:12:16.07	32:32:11.0	0.24771	19.32	1.137	-19.60	-20.67	9.85	-39.36	0.31	-58.97	0.39
r2612_06	vmf132	13:12:10.39	32:30:03.0	0.24954	17.28	1.477	-21.30	-22.70	10.74	1.87	0.14	0.97	0.09
r2612_17	vmf132	13:11:45.80	32:31:21.7	0.24628	17.93	1.579	-20.50	-22.02	10.50	0.97	0.22	1.33	0.12
r2621_03	vmf132	13:11:01.05	32:30:41.6	0.24128	18.35	1.479	-20.12	-21.54	10.29	1.20	0.21	1.89	0.12
r2621_04	vmf132	13:11:02.92	32:29:36.0	0.24061	19.36	1.538	-19.04	-20.52	9.89	0.66	0.40	-0.07	0.20
r2621_11	vmf132	13:11:13.29	32:28:50.9	0.23976	18.63	1.575	-19.73	-21.24	10.19	4.32	0.27	1.15	0.13
r2621_13	vmf132	13:11:17.64	32:28:11.0	0.24181	17.92	1.516	-20.52	-21.98	10.47	3.18	0.18	0.22	0.10
r2621_22	vmf132	13:11:33.84	32:29:11.9	0.25032	18.17	1.536	-20.36	-21.83	10.41	-2.56	0.23	-4.01	0.13
r2631_21	vmf132	13:10:43.33	32:27:04.1	0.24590	17.35	1.448	-21.22	-22.60	10.70	-3.50	0.33	-7.80	0.25
r2631_08	vmf132	13:10:25.08	32:28:44.7	0.25008	19.30	1.361	-19.41	-20.70	9.92	....	....	-1.35	0.28
r2632_07	vmf132	13:10:25.93	32:30:15.4	0.24461	18.82	1.505	-19.68	-21.10	10.12	-0.94	0.83	-3.46	0.24
r2632_13	vmf132	13:10:37.82	32:27:15.2	0.24566	18.34	1.486	-20.19	-21.60	10.31	-0.17	0.19	1.18	0.12
r2641_10	vmf132	13:10:04.73	32:20:51.1	0.24818	17.47	1.469	-21.10	-22.50	10.66	9.17	1.56	-5.42	0.54
ba_29	vmf132	13:09:49.99	32:22:41.0	0.24954	19.77	0.784	-19.55	-20.25	9.52	-53.59	1.20	-61.71	2.16
r2811_06	vmf73	09:43:52.61	16:44:40.1	0.25382	17.82	1.544	-20.73	-22.20	10.56	-6.83	1.17	-3.35	0.36
r2811_16	vmf73	09:43:58.38	16:41:09.6	0.25266	16.96	1.438	-21.70	-23.04	10.87	-0.16	0.65	-2.47	0.24
r2811_18	vmf73	09:43:53.52	16:40:23.1	0.25161	18.32	1.553	-20.21	-21.68	10.36	0.80	1.17	0.43	0.33
r2811_19	vmf73	09:43:58.81	16:40:02.3	0.25384	18.60	1.386	-20.12	-21.42	10.22	-1.26	2.62	0.70	0.67
r2811_20	vmf73	09:44:03.21	16:39:48.5	0.25736	18.81	1.339	-19.98	-21.24	10.14	5.85	3.06	-1.53	0.88

Table 3. Continued.

(1) ID	(2) membership	(3) RA	(4) DEC	(5) z	(6) I [mag]	(7) V-I [mag]	(8) M_B [mag]	(9) M_R [mag]	(10) log(M_*) [$M_\odot$]	(11) [OII] [Å]	(12) E([OII]) [Å]	(13) Hα [Å]	(14) E(Hα) [Å]
r2811_24	vmf73	09:44:01.37	16:38:01.1	0.25355	17.73	1.456	-20.91	-22.28	10.57	4.65	1.30	0.76	0.35
r2811_25	vmf73	09:43:59.68	16:37:30.1	0.25423	18.10	1.536	-20.47	-21.93	10.46	-5.85	1.51	-2.06	0.46
r2812_05	vmf73	09:44:05.00	16:38:34.3	0.25614	18.31	1.465	-20.35	-21.74	10.37	8.83	3.26	-0.05	0.45
r2812_09	vmf73	09:44:00.32	16:40:11.5	0.24866	18.70	1.319	-20.03	-21.27	10.14	5.74	3.73	-1.70	0.82
r2812_12	vmf73	09:43:59.37	16:41:09.9	0.25700	17.26	1.516	-21.35	-22.78	10.78	1.88	1.44	-2.53	0.26
r2812_14	vmf73	09:43:53.57	16:41:43.2	0.25292	17.19	1.430	-21.47	-22.80	10.77	1.48	1.28	1.53	0.28
r2821_02	vmf73	09:43:58.08	16:41:17.0	0.25200	16.67	1.469	-21.95	-23.33	11.00	-0.11	1.40	1.92	0.37
r2821_08	vmf73	09:43:48.71	16:40:39.1	0.25456	17.87	0.823	-21.45	-22.22	10.33	-33.96	0.81	-69.22	1.50
r2821_12	vmf73	09:43:43.00	16:40:34.5	0.25734	17.64	1.488	-21.00	-22.42	10.63	-3.06	1.44	-0.93	0.43
r2821_17	vmf73	09:43:36.34	16:36:57.3	0.25693	17.58	1.503	-21.04	-22.46	10.65	3.38	2.29	-2.92	0.58
r2821_14	vmf73	09:43:40.07	16:39:23.6	0.25781	18.45	1.460	-20.22	-21.62	10.31	4.93	3.98	-3.89	0.83
r2821_20	vmf73	09:43:33.63	16:39:06.8	0.25295	17.80	1.467	-20.83	-22.19	10.54	-13.73	2.82	3.80	0.80
r2821_21	vmf73	09:43:32.42	16:40:01.0	0.25389	18.55	1.477	-20.08	-21.47	10.26	0.92	2.23	1.63	0.74
r2821_27	vmf73	09:43:23.53	16:39:46.4	0.25767	17.98	1.298	-20.85	-22.09	10.45	-0.29	1.31	-3.83	0.54
r2821_29	vmf73	09:43:19.34	16:38:08.6	0.25733	17.87	1.430	-20.83	-22.19	10.53	-5.97	1.61	0.11	0.69
r2822_01	vmf73	09:43:58.93	16:39:22.0	0.25607	18.91	1.398	-19.81	-21.14	10.11	-0.27	0.96	1.26	0.34
r2822_03	vmf73	09:43:56.35	16:36:51.1	0.25523	17.57	1.363	-21.19	-22.49	10.64	2.69	0.64	1.52	0.36
r2822_04	vmf73	09:43:55.89	16:40:36.0	0.25507	18.68	1.394	-20.05	-21.38	10.21	0.97	1.08	2.27	0.32
r2822_05	vmf73	09:43:53.38	16:39:59.1	0.25108	17.73	1.382	-20.98	-22.29	10.56	-0.15	0.45	-2.38	0.17
r2822_06	vmf73	09:43:51.72	16:41:45.0	0.25285	18.03	1.186	-20.89	-21.96	10.37	-2.82	0.50	-16.58	0.30
r2822_09	vmf73	09:43:45.55	16:41:30.9	0.25137	18.83	0.973	-20.32	-21.21	10.01	-19.19	0.67	-22.61	0.55
r2822_14	vmf73	09:43:38.75	16:38:55.5	0.25331	18.59	1.415	-20.09	-21.41	10.22	3.89	0.90	2.31	0.29
r2822_15	vmf73	09:43:37.97	16:39:32.6	0.25742	17.00	1.493	-21.64	-23.06	10.89	4.35	0.56	1.01	0.16
r2822_16	vmf73	09:43:36.80	16:41:02.7	0.25521	18.19	1.427	-20.50	-21.87	10.41	0.76	0.82	0.47	0.25
r2822_17	vmf73	09:43:34.09	16:40:36.1	0.25003	19.08	1.328	-19.67	-20.92	10.01	-1.62	0.88	-0.11	0.35
r2822_19	vmf73	09:43:30.57	16:38:56.0	0.25294	19.30	1.418	-19.38	-20.69	9.93	2.32	1.27	3.04	0.48
r2822_20	vmf73	09:43:29.64	16:40:56.8	0.25775	19.36	1.101	-19.66	-20.71	9.86	1.58	0.65	0.46	0.40
r2822_22	vmf73	09:43:25.34	16:39:07.2	0.25491	17.81	1.494	-20.81	-22.24	10.57	2.17	0.52	0.26	0.17
r2822_23	vmf73	09:43:24.51	16:39:52.1	0.26135	18.46	1.281	-20.44	-21.65	10.28	13.14	1.26	1.88	0.50
r2822_25	vmf73	09:43:22.06	16:39:07.9	0.25037	18.54	1.402	-20.14	-21.46	10.24	-1.78	0.67	-4.66	0.26
r2831_03	vmf73	09:43:22.88	16:41:14.8	0.24829	18.39	1.205	-20.47	-21.60	10.25	-24.22	5.22	-16.09	1.77
r2831_10	vmf73	09:43:08.02	16:42:45.4	0.25696	18.24	1.102	-20.78	-21.80	10.28	-10.66	1.02	-18.04	0.78
r2831_13	vmf73	09:43:01.49	16:42:27.7	0.25601	17.15	1.416	-21.56	-22.90	10.81	4.92	1.29	-1.09	0.36
r2841_07	vmf73	09:44:41.05	16:29:19.5	0.25003	18.64	1.176	-20.27	-21.37	10.14	-45.76	2.52	-21.50	0.73
r2841_10	vmf73	09:44:36.52	16:27:31.5	0.25381	18.10	1.303	-20.70	-21.92	10.39	-14.14	0.75	-11.00	0.28
r2841_17	vmf73	09:44:23.76	16:31:47.1	0.25035	18.12	1.383	-20.57	-21.88	10.39	1.61	0.98	1.43	0.22
r2851_04	vmf73	09:43:50.60	16:28:20.5	0.25065	18.57	0.995	-20.54	-21.47	10.11	-12.13	0.56	-28.68	0.72
r2851_14	vmf73	09:44:04.69	16:32:49.3	0.25340	19.02	1.446	-19.63	-20.98	10.05	3.75	2.19	-4.63	0.66
r2851_17	vmf73	09:43:52.24	16:34:00.8	0.25195	17.70	1.405	-20.99	-22.30	10.57	1.31	0.55	0.78	0.18
r2811_01	vmf74	09:43:44.47	16:46:05.3	0.17837	17.66	1.323	-20.18	-21.42	10.20	4.45	0.72	1.37	0.24
r2811_03	vmf74	09:43:43.51	16:45:20.1	0.18029	18.27	1.278	-19.68	-20.87	9.97	2.27	0.97	0.85	0.33
r2811_05	vmf74	09:43:44.49	16:44:54.2	0.18009	18.50	1.183	-19.57	-20.65	9.85	-21.52	1.18	-77.27	1.12
r2811_07	vmf74	09:43:46.72	16:44:25.2	0.17917	18.19	1.198	-19.84	-20.92	9.96	-2.13	1.22	-2.40	0.40
r2811_08	vmf74	09:43:45.15	16:44:05.6	0.17884	18.53	1.268	-19.40	-20.56	9.84	-8.10	1.85	-8.58	0.53
r2811_10	vmf74	09:43:55.55	16:43:34.6	0.17876	18.04	1.286	-19.86	-21.05	10.04	0.93	1.33	0.97	0.34
r2811_11	vmf74	09:43:49.12	16:43:21.2	0.18086	16.81	1.354	-21.03	-22.33	10.57	0.70	0.64	-1.23	0.18
r2811_13	vmf74	09:43:53.02	16:42:48.2	0.17838	18.68	1.218	-19.30	-20.42	9.77	2.84	2.04	1.52	0.59
r2811_14	vmf74	09:43:58.75	16:42:02.5	0.18250	17.82	1.305	-20.11	-21.34	10.16	5.52	1.71	1.56	0.36
r2811_22	vmf74	09:43:43.31	16:39:18.5	0.17701	18.46	1.025	-19.73	-20.69	9.82	-21.35	2.32	-25.48	0.99
r2811_23	vmf74	09:43:59.52	16:38:29.8	0.17833	17.98	1.123	-20.12	-21.14	10.02	-2.49	0.96	-6.81	0.28
r2812_02	vmf74	09:43:43.06	16:37:36.0	0.18249	17.68	1.344	-20.20	-21.47	10.22	-0.22	1.36	-0.52	0.21
r2812_16	vmf74	09:44:01.02	16:42:04.1	0.17750	17.95	1.203	-20.03	-21.16	10.07	-16.80	4.23	-10.69	0.60
r2812_17	vmf74	09:43:45.13	16:42:46.3	0.18134	17.26	1.307	-20.66	-21.90	10.39	6.09	1.68	-4.01	0.24
r2812_22	vmf74	09:43:43.45	16:44:31.8	0.18096	17.77	1.289	-20.18	-21.39	10.18	8.73	3.08	0.07	0.36
r2812_21	vmf74	09:43:44.86	16:44:02.2	0.17932	17.70	1.340	-20.14	-21.39	10.19	-6.10	1.10	-9.78	0.25
r2821_03	vmf74	09:43:56.38	16:39:57.5	0.17992	18.21	1.239	-19.77	-20.92	9.97	10.57	3.86	-0.03	0.71
r2821_06	vmf74	09:43:51.14	16:37:26.3	0.17486	18.72	0.891	-19.70	-20.37	9.55	-23.75	2.87	-31.60	2.05
r2821_07	vmf74	09:43:50.04	16:39:54.7	0.17926	18.60	1.319	-19.27	-20.49	9.83	-3.49	4.05	2.84	0.91
r2821_09	vmf74	09:43:47.69	16:39:10.2	0.17974	18.67	1.258	-19.29	-20.45	9.79	-5.83	6.46	0.17	1.12
r2821_10	vmf74	09:43:46.04	16:39:54.5	0.17763	18.76	1.285	-19.11	-20.33	9.76	-16.78	7.64	1.04	1.10
r2821_11	vmf74	09:43:44.53	16:39:19.8	0.17656	17.73	1.256	-20.17	-21.36	10.15	-6.26	2.14	-0.59	0.49
r2822_07	vmf74	09:43:49.72	16:40:51.4	0.18048	17.63	1.306	-20.28	-21.51	10.23	4.17	0.58	1.07	0.15
r2822_10	vmf74	09:43:44.15	16:40:47.1	0.17948	18.43	1.307	-19.46	-20.67	9.90	-0.03	0.80	-0.40	0.20
r2822_13	vmf74	09:43:39.73	16:37:22.5	0.17946	19.23	1.161	-18.85	-19.89	9.54	1.35	1.87	-14.50	0.45
r2831_09	vmf74	09:43:08.92	16:41:44.8	0.18137	18.21	1.415	-19.57	-20.93	10.03	-14.13	2.55	-19.38	0.88
r2831_20	vmf74	09:42:44.14	16:45:34.9	0.17989	18.08	1.173	-19.99	-21.06	10.00	-5.48	1.19	-2.32	0.60
r2841_03	vmf74	09:44:54.15	16:28:00.6	0.18333	19.13	1.096	-19.07	-20.07	9.58	-27.04	8.74	-17.81	0.82
r2841_08	vmf74	09:44:40.09	16:30:59.7	0.18478	19.32	1.081	-18.93	-19.93	9.52	-21.39	1.97	-28.51	0.92
r2841_20	vmf74	09:44:16.29	16:28:47.4	0.18157	19.46	0.910	-18.97	-19.78	9.39	-28.28	2.91	-13.70	1.07
r2851_09	vmf74	09:43:50.52	16:30:28.0	0.18124	19.09	1.184	-19.00	-20.10	9.63	0.54	2.14	-0.59	0.77
r2851_10	vmf74	09:43:48.57	16:30:39.7	0.17962	18.58	0.794	-19.95	-20.62	9.64	-29.97	0.65	-41.39	0.65
r2851_11	vmf74	09:43:52.55	16:31:20.4	0.18176	19.32	1.128	-18.84	-19.87	9.52	-39.42	1.39	-65.98	1.24
r2851_19	vmf74	09:43:59.00	16:35:02.8	0.18102	19.39	0.904	-19.05	-19.86	9.42	-5.48	1.62	-17.97	0.64
r2221_09	group1	17:26:29.54	74:29:34.7	0.05308	16.30	1.114	-18.89	-19.96	9.52	....	....	-13.81	0.16
r2222_11	group1	17:26:18.59	74:30:54.1	0.05278	18.65	0.844	-16.97	-17.74	8.53	....	....	....	....
r2231_18	group1	17:25:26.20	74:30:15.5	0.05219	17.48	0.835	-18.12	-18.89	8.98	....	....	-9.51	0.12
r2222_20	group1	17:26:15.09	74:25:49.2	0.05292	17.89	0.781	-17.81	-18.54	8.79	....	....	-38.39	0.13
r2221_08	group2	17:27:07.02	74:30:29.4	0.04385	18.36	0.940	-16.73	-17.57	8.48	....	....	-41.37	0.46
r2221_11	group2	17:27:07.97	74:28:40.5	0.04208	16.99	0.866	-18.08	-18.88	8.97	....	....	-21.11	0.26
r2222_18	group2	17:26:45.45	74:27:01.2	0.04405	19.21	0.657	-16.34	-16.92	8.06	....	....	-51.86	0.39

Table 3. Continued.

(1) ID	(2) membership	(3) RA	(4) DEC	(5) z	(6) I [mag]	(7) V-I [mag]	(8) M_B [mag]	(9) M_R [mag]	(10) log(M_*) [$M_\odot$]	(11) [OII] [Å]	(12) E([OII]) [Å]	(13) Hα [Å]	(14) E(Hα) [Å]
r2231_08	group2	17:24:25.65	74:28:34.5	0.04191	17.38	0.734	-17.87	-18.56	8.77	....	....	-65.83	0.15
r2231_19	group2	17:25:34.22	74:28:54.1	0.04133	17.43	0.962	-17.42	-18.34	8.81	....	....	-8.52	0.11
r2211_11	group3	17:29:41.54	74:42:31.7	0.24259	18.30	1.285	-20.41	-21.62	10.27	-14.98	0.38	-20.88	0.24
r2211_13	group3	17:29:48.60	74:42:15.0	0.24404	17.93	1.503	-20.56	-21.99	10.47	3.07	1.35	2.55	0.38
r2211_17	group3	17:30:02.07	74:41:43.3	0.24405	17.85	1.333	-20.83	-22.08	10.46	-5.01	0.70	-9.60	0.30
r2211_19	group3	17:30:09.69	74:42:44.1	0.24513	18.45	1.431	-20.14	-21.49	10.25	-6.01	0.45	-4.50	0.21
r2211_20	group3	17:30:13.48	74:41:02.5	0.24471	17.89	1.476	-20.65	-22.04	10.48	7.76	1.19	-0.52	0.28
r2211_21	group3	17:30:16.74	74:42:26.8	0.24230	18.69	1.510	-19.76	-21.21	10.17	5.14	0.64	3.05	0.24
r2212_11	group3	17:29:40.88	74:41:23.3	0.24196	18.12	1.467	-20.38	-21.78	10.38	4.51	1.89	1.80	0.64
r2242_18	group3	17:24:31.58	74:37:39.2	0.24194	18.17	1.709	-20.06	-21.72	10.41	-13.17	1.00	-2.97	0.21
r2621_01	group4	13:10:52.83	32:30:58.0	0.18687	19.30	1.355	-18.63	-20.03	9.68	-8.00	0.40	-19.11	0.22
r2631_16	group4	13:10:37.26	32:26:37.6	0.18599	17.17	1.017	-21.14	-22.14	10.26	-20.02	0.25	-27.48	0.30
r2631_11	group4	13:10:30.08	32:29:10.8	0.18727	16.42	1.478	-21.43	-22.93	10.89	0.63	0.28	1.87	0.14
r2631_01	group4	13:10:09.80	32:29:44.2	0.18593	18.05	1.416	-19.91	-21.28	10.20	2.90	0.38	0.17	0.18
r2632_15	group4	13:10:39.83	32:28:42.5	0.18635	17.39	1.538	-20.47	-21.96	10.43	-0.51	0.19	-2.62	0.08
r2211_01	field	17:28:35.55	74:43:18.4	0.32074	18.43	1.319	-21.01	-22.24	10.52	-10.68	0.38	-15.00	0.40
r2211_02	field	17:28:46.44	74:42:38.1	0.19443	18.45	0.983	-20.01	-20.93	9.90	-10.03	0.38	-13.96	0.25
r2211_04	field	17:29:01.00	74:40:07.9	0.27259	18.76	1.594	-19.96	-21.47	10.28	6.43	0.75	-6.25	0.30
r2211_12	field	17:29:45.21	74:40:22.0	0.15859	16.18	1.330	-21.36	-22.63	10.68	....	....	....	....
r2211_15	field	17:29:53.77	74:39:44.1	0.15745	17.39	1.226	-20.31	-21.42	10.15	....	....	-6.20	0.25
r2211_16	field	17:29:59.01	74:41:08.1	0.33182	18.09	1.178	-21.57	-22.66	10.65	-29.21	0.52	-30.22	1.14
r2211_18	field	17:30:05.41	74:40:00.7	0.15708	18.60	1.324	-18.97	-20.17	9.69	....	....	-3.98	0.41
r2211_22	field	17:30:22.64	74:39:20.9	0.34028	18.94	1.821	-20.31	-21.95	10.49	2.62	0.59	-0.04	0.45
r2211_24	field	17:30:45.34	74:41:21.3	0.31546	18.73	1.589	-20.44	-21.91	10.45	0.20	0.46	2.05	0.41
r2212_12	field	17:29:43.86	74:41:45.9	0.15985	18.38	0.975	-19.63	-20.51	9.71	-30.89	0.95	....	....
r2212_14	field	17:29:50.08	74:42:24.7	0.24585	17.73	1.429	-20.86	-22.22	10.55	-6.09	0.50	-5.65	0.25
r2212_16	field	17:30:00.75	74:42:09.0	0.27302	19.24	1.511	-19.56	-21.00	10.08	-2.40	1.02	3.05	0.81
r2212_19	field	17:30:18.14	74:41:44.4	0.33812	18.31	1.818	-20.91	-22.54	10.73	2.78	0.72	-3.66	0.65
r2221_04	field	17:27:06.87	74:32:15.8	0.28072	18.32	0.985	-21.03	-22.01	10.33	....	....	-46.66	1.04
r2221_13	field	17:26:25.30	74:27:56.1	0.22819	18.78	1.348	-19.70	-20.96	10.03	-8.97	1.04	-15.25	0.47
r2222_01	field	17:26:43.68	74:35:29.1	0.50080	19.36	1.680	-21.34	-22.69	10.71	-2.40	0.33	....	....
r2222_02	field	17:27:26.70	74:34:42.8	0.18050	19.03	1.057	-19.21	-20.16	9.60	-70.67	1.25	-13.85	0.18
r2222_04	field	17:26:24.13	74:33:53.7	0.28905	19.12	1.227	-20.12	-21.29	10.12	-7.08	0.30	-22.98	0.37
r2222_05	field	17:27:22.22	74:32:27.3	0.24178	19.18	0.881	-19.94	-20.76	9.78	-18.68	0.31	-19.77	0.22
r2222_06	field	17:26:46.66	74:32:13.2	0.55816	19.24	1.698	-21.80	-23.14	10.88	-10.19	0.27	....	....
r2222_08	field	17:26:54.96	74:31:35.9	0.27059	18.07	1.020	-21.16	-22.14	10.41	-0.55	0.24	10.24	0.62
r2222_09	field	17:27:09.38	74:31:12.9	0.65900	19.26	2.406	-22.20	-23.83	11.23	-5.89	0.68	0.00	0.00
r2222_12	field	17:26:53.67	74:29:57.5	0.54749	19.25	2.087	-21.61	-23.16	10.95	-3.17	0.47	....	....
r2222_13	field	17:26:33.10	74:29:40.5	0.29010	18.91	1.662	-19.93	-21.49	10.30	-5.43	0.36	2.56	0.24
r2222_15	field	17:26:10.37	74:29:09.5	0.18043	18.17	1.046	-20.08	-21.02	9.94	-25.86	0.34	-29.13	0.18
r2222_17	field	17:26:59.73	74:27:27.3	0.41500	19.26	1.977	-20.60	-22.26	10.62	1.51	0.37	-10.05	0.41
r2231_06	field	17:24:14.39	74:29:43.0	0.21837	19.06	0.920	-19.78	-20.61	9.73	-25.41	0.51	-26.11	0.43
r2231_07	field	17:24:20.53	74:28:13.3	0.54921	19.14	1.646	-21.89	-23.17	10.87	-8.90	0.25	....	....
r2231_11	field	17:24:37.73	74:30:13.6	0.18489	19.49	1.168	-18.65	-19.75	9.49	-48.04	0.78	-32.86	0.40
r2231_13	field	17:24:57.93	74:29:05.6	0.43546	18.32	1.913	-21.77	-23.33	11.03	0.84	0.23	....	....
r2231_16	field	17:25:12.29	74:29:40.6	0.29537	19.17	1.210	-20.12	-21.26	10.11	-19.73	0.31	-48.69	0.45
r2231_23	field	17:25:54.24	74:26:49.6	0.34361	18.36	1.546	-21.11	-22.52	10.67	-1.55	0.29	-8.67	0.65
r2241_02	field	17:23:27.27	74:46:43.8	0.44623	18.36	2.172	-21.68	-23.40	11.09	4.18	0.47	....	....
r2241_04	field	17:24:15.13	74:45:07.0	0.43284	18.39	1.686	-21.81	-23.21	10.94	-7.59	0.32	....	....
r2241_11	field	17:23:55.07	74:42:40.0	0.33892	18.45	1.800	-20.79	-22.40	10.66	-9.00	0.91	0.97	0.44
r2241_14	field	17:24:12.80	74:40:47.1	0.18050	17.48	1.381	-20.33	-21.65	10.31	-5.11	2.25	0.67	0.27
r2241_20	field	17:23:50.33	74:38:39.8	0.04373	18.69	1.516	-15.32	-16.93	8.48	....	....	-11.48	0.19
r2241_21	field	17:23:54.90	74:38:24.1	0.26848	17.01	0.754	-22.46	-23.19	10.70	-17.10	0.32	-36.41	0.29
r2241_22	field	17:23:47.22	74:38:01.9	0.24012	17.91	1.212	-20.84	-21.98	10.39	2.47	0.58	1.78	0.18
r2242_03	field	17:23:39.55	74:45:22.9	0.42995	19.34	1.555	-20.90	-22.23	10.52	-13.05	0.48	-50.55	1.95
r2242_07	field	17:23:37.38	74:43:40.0	0.29567	18.02	1.610	-20.93	-22.43	10.66	1.50	0.67	0.67	0.25
r2242_10	field	17:23:51.86	74:42:56.3	0.20966	19.04	1.696	-18.79	-20.45	9.90	3.91	2.31	-0.35	0.28
r2242_11	field	17:24:02.24	74:42:37.0	0.33906	18.85	1.709	-20.46	-22.00	10.49	-0.95	0.99	-3.18	0.40
r2242_12	field	17:23:13.33	74:42:15.4	0.29681	18.90	1.691	-19.99	-21.57	10.33	-0.22	0.90	1.00	0.36
r2242_13	field	17:23:17.51	74:40:37.5	0.18069	18.01	1.095	-20.18	-21.18	10.02	-5.53	0.39	-21.72	0.21
r2251_02	field	17:23:53.84	74:23:11.3	0.19508	18.20	1.284	-19.89	-21.15	10.09	4.56	2.45	0.26	0.24
r2251_06	field	17:23:50.15	74:20:50.9	0.05868	18.68	0.877	-17.14	-17.94	8.61	....	0.00	-26.72	0.30
r2251_08	field	17:24:12.25	74:19:17.4	0.22829	18.58	0.903	-20.39	-21.21	9.96	-20.21	0.80	-27.68	0.36
r2251_10	field	17:24:04.79	74:18:39.2	0.44273	18.39	0.822	-22.37	-23.16	10.67	-5.02	0.14	-21.15	0.35
r2251_11	field	17:25:05.54	74:17:51.8	0.04355	16.66	1.012	-18.29	-19.21	9.17	....	0.00	-10.18	0.16
r2251_15	field	17:24:45.55	74:15:44.8	0.06325	18.35	0.743	-17.81	-18.51	8.77	....	0.00	-11.96	0.30
r2251_16	field	17:24:54.82	74:15:13.7	0.29141	16.71	1.161	-22.60	-23.67	11.03	-12.12	0.75	-1.42	0.25
r2611_02	field	13:12:15.56	32:33:06.4	0.26403	18.93	1.349	-20.04	-21.39	10.17	-8.30	0.40	-23.45	0.37
r2611_03	field	13:12:10.01	32:32:04.4	0.13084	18.81	1.000	-18.62	-19.70	9.35	-24.90	0.61	-28.72	0.26
r2611_07	field	13:12:02.58	32:31:35.8	0.43572	18.12	2.142	-21.96	-23.59	11.15	1.37	0.36	-1.01	0.55
r2611_11	field	13:11:54.78	32:30:38.6	0.15710	18.72	0.935	-19.24	-20.21	9.49	-13.09	0.37	-10.49	0.23
r2611_16	field	13:11:46.33	32:32:54.9	0.35143	18.08	1.796	-21.23	-22.78	10.83	3.52	0.33	3.01	0.31
r2612_01	field	13:12:28.82	32:30:27.7	0.26270	19.01	1.600	-19.73	-21.25	10.23	0.00	0.27	-0.05	0.18
r2612_03	field	13:12:18.72	32:30:40.0	0.49186	19.47	1.650	-21.44	-22.44	10.39	-12.58	0.18	....	....
r2612_09	field	13:12:04.96	32:31:56.8	0.36498	19.11	1.346	-20.85	-22.13	10.47	-11.92	0.19	-14.38	0.26
r2612_11	field	13:12:01.09	32:31:31.0	0.43522	19.02	2.049	-21.37	-22.91	10.92	1.11	0.22	1.50	0.37
r2612_12	field	13:11:59.85	32:31:24.2	0.43773	18.74	2.075	-21.56	-23.13	10.93	1.68	0.20	0.00	0.33
r2612_14	field	13:11:52.16	32:32:12.1	0.44078	18.83	2.091	-21.50	-22.91	10.86	2.98	0.21	-5.77	0.32
r2612_19	field	13:11:42.75	32:32:26.2	0.14883	16.72	1.208	-21.00	-22.09	10.33	-13.62	0.15	-20.03	0.08
r2621_02	field	13:10:57.07	32:28:05.7	0.12024	18.68	1.209	-18.33	-19.57	9.51	-1.12	0.60	-10.26	0.13

Table 3. Continued.

(1) ID	(2) membership	(3) RA	(4) DEC	(5) z	(6) I [mag]	(7) V-I [mag]	(8) M_B [mag]	(9) M_R [mag]	(10) log(M_*) [$M_\odot$]	(11) [OII] [Å]	(12) E([OII]) [Å]	(13) Hα [Å]	(14) E(Hα) [Å]
r2621_05	field	13:11:04.39	32:32:09.8	0.15807	18.69	0.962	-19.38	-20.34	9.36	....	....	-1.37	0.13
r2621_06	field	13:11:05.84	32:29:57.6	0.30678	18.87	1.875	-19.98	-21.76	10.45	-3.45	0.27	-1.38	0.17
r2621_09	field	13:11:10.48	32:29:39.1	0.23464	19.41	1.383	-19.30	-20.53	9.82	-2.30	0.30	-7.58	0.19
r2621_10	field	13:11:12.39	32:32:06.0	0.30175	18.37	1.359	-21.15	-22.32	10.49	-9.52	0.17	-12.55	0.16
r2621_12	field	13:11:14.83	32:30:59.0	0.30721	18.38	1.630	-21.00	-22.43	10.66	-3.89	0.15	-3.95	0.13
r2621_18	field	13:11:28.25	32:28:06.1	0.43404	18.58	2.144	-21.45	-23.28	11.03	-4.27	0.23	....	....
r2631_02	field	13:10:15.66	32:27:22.0	0.18490	16.26	1.483	-21.62	-23.04	10.87	-4.72	0.21	-0.55	0.09
r2631_03	field	13:10:16.97	32:29:06.1	0.12306	16.99	1.228	-20.25	-21.28	10.02	....	....	-11.70	0.27
r2631_04	field	13:10:18.44	32:27:39.6	0.12364	17.01	1.292	-19.89	-21.28	10.08	....	....	-25.65	0.19
r2631_05	field	13:10:19.66	32:29:34.4	0.25985	18.90	1.514	-20.00	-21.00	9.75	-57.95	1.65	-8.50	0.40
r2631_10	field	13:10:28.21	32:26:18.3	0.15738	18.66	0.987	-19.22	-20.26	9.63	-31.05	0.58	0.25	0.35
r2632_01	field	13:10:09.53	32:26:28.6	0.12557	18.07	1.184	-19.04	-20.25	9.73	....	....	....	....
r2632_04	field	13:10:20.31	32:27:23.8	0.12333	19.12	0.829	-18.20	-19.11	9.14	....	....	-23.07	0.18
r2632_05	field	13:10:23.46	32:29:52.4	0.40813	19.41	1.099	-20.92	-21.75	10.00	-36.95	0.27	....	....
r2632_06	field	13:10:24.87	32:27:36.1	0.18508	17.35	1.446	-20.46	-21.94	10.48	-1.76	0.27	-2.10	0.11
r2632_14	field	13:10:38.86	32:28:04.1	0.30783	19.37	1.571	-19.69	-21.14	10.06	-23.37	1.36	-16.20	1.24
r2632_18	field	13:10:50.60	32:30:19.7	0.40243	19.13	1.944	-20.62	-22.54	10.79	-1.45	0.23	....	....
r2641_11	field	13:10:03.30	32:21:30.2	0.28419	18.66	1.508	-20.38	-21.83	10.44	-13.38	1.20	-39.16	2.26
r2651_01	field	13:10:32.47	32:19:15.3	0.28500	19.42	1.513	-19.47	-20.90	10.10	1.53	0.34	2.22	0.30
r2651_03	field	13:10:40.07	32:20:47.8	0.55177	18.00	1.669	-23.20	-24.32	11.22	-14.19	0.11	....	....
r2651_04	field	13:10:42.49	32:16:34.9	0.12691	16.04	1.423	-20.79	-22.27	10.59	-0.13	0.19	-3.65	0.04
r2651_07	field	13:10:46.66	32:21:16.7	0.30771	18.66	1.317	-20.69	-22.01	10.44	0.53	0.18	0.38	0.17
r2651_10	field	13:10:56.84	32:17:15.9	0.14591	18.12	1.154	-19.38	-20.58	9.86	....	....	-0.87	0.11
r2651_11	field	13:10:59.78	32:18:39.0	0.40701	18.66	1.716	-21.32	-22.73	10.76	-3.53	0.18	....	....
r2651_12	field	13:11:01.13	32:18:08.6	0.40683	17.94	2.069	-21.73	-23.53	11.15	2.65	0.18	....	....
r2651_13	field	13:11:07.05	32:17:24.8	0.40657	18.66	2.031	-21.48	-22.96	10.85	2.88	0.24	....	....
r2651_16	field	13:11:12.51	32:18:42.8	0.60652	19.00	1.880	-22.22	-23.46	10.78	-10.59	0.22	....	....
r2811_12a	field	09:43:58.66	16:43:04.5	0.16614	18.56	0.943	-19.73	-20.44	9.39	....	....	-45.42	1.74
r2812_19	field	09:43:51.27	16:43:11.2	0.15433	18.95	0.659	-18.88	-19.72	9.52	-26.92	1.21	-34.63	0.75
r2812_23	field	09:43:55.30	16:44:48.9	0.16487	18.46	1.398	-19.09	-20.51	9.91	12.44	7.53	4.62	0.50
r2812_25	field	09:43:55.77	16:45:33.8	0.15788	19.10	1.155	-18.61	-19.84	9.61	-1.11	7.84	....	....
r2812_26	field	09:43:51.93	16:45:45.2	0.21565	19.33	1.746	-18.67	-20.54	9.73	....	....	-0.58	1.05
r2821_05	field	09:43:53.29	16:41:20.1	0.07725	17.93	0.764	-16.26	-17.16	8.22	....	....	-69.03	0.65
r2821_23	field	09:43:28.76	16:37:53.2	0.18995	18.08	1.182	-20.06	-21.27	10.19	0.77	2.50	3.92	1.62
r2821_28	field	09:43:22.54	16:38:53.6	0.27333	17.90	1.451	-21.09	-22.48	10.67	-5.03	1.22	-19.08	0.83
r2822_24	field	09:43:23.20	16:40:38.3	0.16715	18.83	1.230	-18.89	-20.24	9.70	-21.56	1.01	-28.55	0.41
r2831_05	field	09:43:19.89	16:42:29.8	0.16724	17.58	1.149	-20.30	-21.52	10.06	-11.15	2.29	-20.93	0.78
r2831_08	field	09:43:12.49	16:44:30.0	0.17047	17.87	1.241	-19.84	-21.31	10.25	....	....	-8.77	0.62
r2831_14	field	09:43:00.57	16:42:17.0	0.14972	16.86	1.207	-20.65	-21.96	10.44	3.67	1.17	-7.81	0.24
r2831_16	field	09:42:56.10	16:41:13.4	0.23116	18.63	1.252	-20.17	-21.21	9.79	-9.85	1.60	-20.22	0.95
r2831_17	field	09:42:52.23	16:42:47.2	0.16275	17.88	1.043	-20.13	-21.18	9.89	-21.33	1.13	-7.25	0.45
r2831_18	field	09:42:51.23	16:41:08.8	0.23352	17.07	1.118	-21.63	-22.86	10.70	-5.96	0.39	-22.38	0.31
r2841_01	field	09:44:58.57	16:30:07.6	0.22351	19.41	1.424	-18.65	-20.22	9.86	0.31	3.79	1.67	0.85
r2841_09	field	09:44:38.51	16:27:52.5	0.23310	17.25	1.330	-21.14	-22.58	10.74	1.08	0.92	-3.37	0.23
r2841_12	field	09:44:33.83	16:30:53.1	0.27388	19.33	0.753	-19.68	-20.73	9.93	-39.60	1.62	-51.65	3.45
r2841_13	field	09:44:32.35	16:28:34.4	0.15980	18.91	1.039	-18.87	-20.08	9.47	-8.75	1.07	....	....
r2841_18	field	09:44:21.95	16:30:48.2	0.23268	19.19	1.459	-19.13	-20.61	9.85	2.60	1.96	-2.44	0.43
r2841_19a	field	09:44:20.00	16:30:28.5	0.23338	17.51	1.290	-21.03	-22.49	10.63	-2.40	0.47	-3.95	0.15
r2851_01b	field	09:43:57.19	16:25:17.4	0.22289	19.09	1.099	-19.41	-20.69	9.99	-26.49	0.94	-33.61	0.94
r2851_06	field	09:44:07.29	16:29:22.8	0.23247	17.24	1.355	-21.25	-22.70	10.73	1.15	0.69	-1.32	0.17
r2851_13	field	09:43:58.24	16:32:18.3	0.22294	18.11	1.310	-20.32	-21.94	10.40	0.25	1.08	0.83	0.29